UNIVERSITY OF BIRMINGHAM

THE EFFECTS OF DAMAGE ON HIGH PRESSURE GAS TURBINE DISC ALLOYS

Industrially Sponsored by Rolls-Royce

by

Benjamin Thomas Spencer Cousins

A thesis submitted to the University of Birmingham for
the degree of Master of Research

School of Metallurgy and Materials
College of Engineering and Physical Sciences
University of Birmingham
November 2011

Abstract

The European Aviation Safety Agency (EASA) mandates appropriate damage tolerance lifing assessments for Critical Group A components. The assessments may be demonstrated by deterministic crack propagation modelling, testing or probabilistic methods. For each critical area a calculated residual life shall be determined for overhaul and interval cycles ensuring safe operation.

During assembly, operation and maintenance routines of the turbine section of gas turbine engines scratch or gouge damage can occur due to component handling. The aim of this project is to assess the damage tolerance of High Pressure Turbine Disc (HPTD) components after the introduction of gouge damage and hence to optimise damage tolerance lifing approaches and minimise component retirements.

Historically, due to the relative hardness of Alloy 720Li, a multi-pass scratching technique has been used to simulate deep in-service scratch damage to HP turbine discs. A single-pass scratching method, which may better represent real-life damage formation, has been used in similar test programmes for IN718, which is comparatively easier to scratch. The reliability of the single-pass technique and estimations of its implications on component life have been assessed as follows:

i). The characterisation of a series of single-pass scratches at different depths. This includes metallurgical sectioning to assess microstructural changes/defects, analysis of the scratch profile conformity using non-contact confocal and optical microscopes.

ii). Low-cycle fatigue (LCF) testing of representative Kt notch feature, shot peened specimens manufactured from disc forgings used for previous multi-pass LCF testing. The tests compare the fatigue properties between single-pass and multi-pass scratch damaged sites with the aid of a D.C.P.D. technique to monitor the initiation and growth of the fatigue cracks, and ultimately identify the main factors that contribute to fatigue life differences.

iii). Fractographic observations, SEM characterisation of the damaged material and microhardness map profiles were produced to assess the surface and sub-surface material states respectively.

Declaration

This is to certify that:

i. the thesis comprises only my original work towards the MRes except where indicated,

ii. due acknowledgement has been made in the text to all other material used,

iii. the thesis is less than 15,000 words in length, excluding tables, headings, bibliographies, appendices and footnotes.

Benjamin Thomas Spencer Cousins

Contents

List of Tables

List of Figure

Chapter 1:

Introduction

Gas turbine technologies are used widely within the aerospace industry in the UK and across the world. Two on-going issues for turbine manufacturers are natural resource limitations and climate change due to gas turbine fuel consumption and CO_2 emissions. The sustainability of the industry and products produced, taking into account the inevitable demand driven growth, necessitates concern by manufacturers and governments alike.

The Engineering and Physical Sciences Research Council (EPSRC) and Rolls-Royce together with the universities of Cambridge, Swansea and Birmingham have formed a strategic partnership. In addition, over 10 other Doctoral Training Centres (DTC) and two Knowledge Transfer Accounts

(KTA) are being funded by over 100 active research grants. These compliment the each other and strengthen Rolls-Royce and other companies' technical capabilities portfolio together with strengthening academic expertise. These programmes span the nuclear industry, energy generation technologies, manufacturing technologies and materials science.

The DTC at Birmingham, which will be the focus of this thesis, concentrates on structural metallic systems for gas turbine applications. There's an estimated one third of UK energy generation capacity and the vast majority of aircraft propulsion provided by gas turbine technology. Manufacturers and states are demanding greater engine efficiencies which impose higher demands on turbine material performance. The focus of this DTC is to address concerns surrounding resource, expertise and CO_2 emissions in terms of the gas turbine industry. The partnership aims to:-

- Perform materials research to improve efficiency and sustainability of gas turbine engines.
- Train the next generation of world-class materials scientists to strengthen UK academia and industry.

This package of research aims to better understand the implications of high pressure turbine discs damage caused by installation or repair scenarios and it implications to component life.

Chapter 2:

The Jet Engine

2.1 Inception

Sir Frank Whittle registered the first patent for a turbojet engine design in 1930 which flew in 1941. During this time Dr Hans von Ohain developed a design which was granted a patent in 1936 and made the first operational flight of a turbojet engine slightly earlier in 1939. The two men are recognised as the co-inventors of jet propelled flight forming the basis of jet engine technology today.

The principals proven by Whittle and von Ohain have since been refined and applied to many motive applications across the civil aerospace, defence and rail industries amongst others. Stationery jet engines used for power generation are common across industry such as energy and marine.

2.2 Thermodynamic Cycle

Jet engines, also called gas turbines, operate according to Newton's Third Law of motion. In terms of jet propelled flight, air enters the engine through a fan at the intake stage. Air flow progresses though a compressor stage to increase pressure. The compressed air is then mixed with fuel which is then ignited. The explosive expansion of gas is channelled through a turbine stage before exiting through a nozzle at the rear, thus propelling the engine at great speeds. The exhaust flow can be scavenged and used for naval ship propeller drives, turbine drives for electrical power generation or compressor pumps for gas pipelines in non-aerospace applications.

Thermodynamic relationships exist between pressure, temperature and volume are applied throughout the engine and form the physical basis for gas turbines. Figure 2-1 shows the Pressure-Volume diagram and the Brayton cycle. These apply Boyle's Law and Charles's Law from stage one air inlet to stage five at the exhaust.

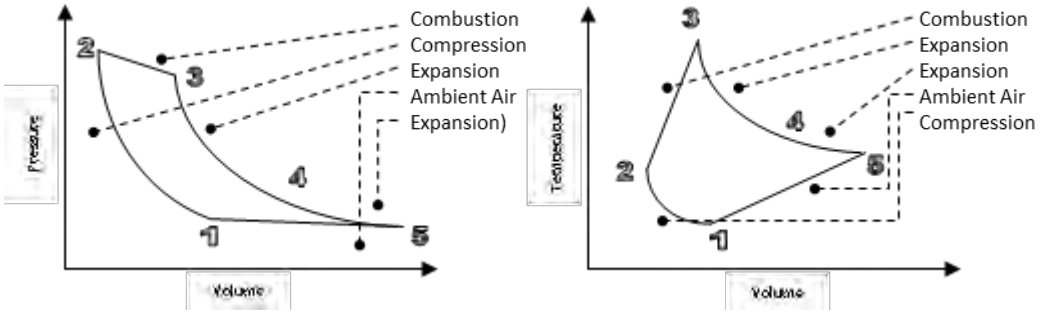

Figure 2-1. Thermodynamic relationships. Pressure-Volume diagram (left) and the Brayton Cycle (right).

2.3 Jet Engine Designs

The three distinct jet engine designs are common in the gas turbine industry. These designs have different applications which suit their performance characteristics, describes below and shown in Figure 2-2.

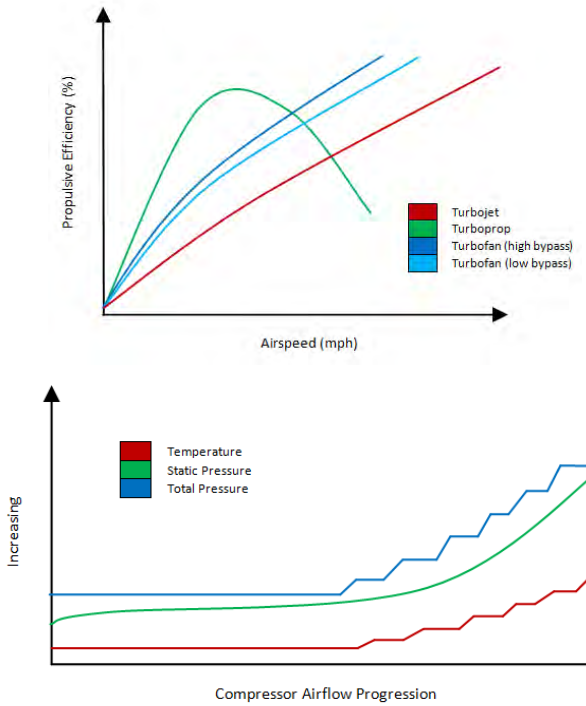

Figure 2-2. Typical gas turbine designs and compressor relationships. Adapted from [1]

2.3.1 Turbojet

This simple engine design can achieve high speeds but at a far lower fuel efficiency. The fuel consumption rate increases faster than the propulsive engine thrust can provide. This is described numerically in equation (1) and (2) which show that thrust (F) varies proportionally according to the velocity of the jet whilst fuel consumption varies with the square of the jet velocity.

$$KE = \frac{1}{2} W V^2{}_{jet} \tag{1}$$

$$F = W\left(v_{jet} - v_{flight}\right) + A\left(p_{exit} - p_{inlet}\right) \tag{2}$$

Therefore, turbojets are suitable for short flights with low Specific Fuel Consumptions (SFC) requirements. Commercially, turbojets exceed imposed noise pollution limitations and do not meet the efficiency requirements for long haul flight fuel economy. Military applications such as Vertical Take Off and Landing (VTOL) capabilities for fighter jets exist because turbojets excel in thrust per unit weight and volume criteria.

Figure 2-3. Turbojet schematic [1]

2.3.2 Turboprop

The turboprop or turboshaft design utilises maximum energy from the exhaust flow which is transmitted to a shroud-less fan system. These are used for Short Take Off and Landing (STOL) capabilities on small commuter aircraft. However, the Airbus A400M also applies the STOL capability on a very large scale.

Turboshaft are typically used for helicopters, navel applications and pipeline technology. The low velocities required for turboshaft applications result in high efficiencies.

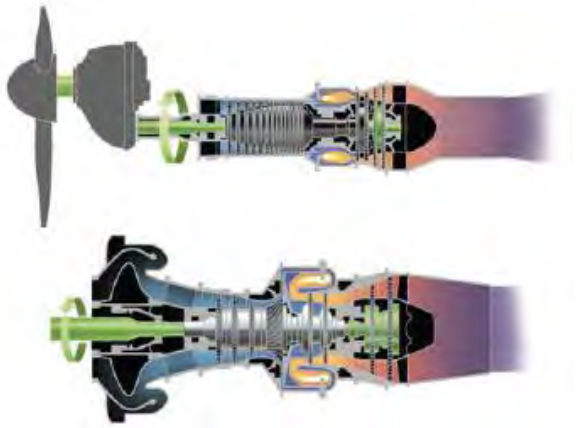

Figure 2-4. Turboprop (top) and Turboshaft (bottom) schematics [1].

2.3.3 Turbofan

Current civil aerospace engines such as the Rolls-Royce Trent family are known as turbofan engines. The turbofan design, see Figure 2-5, uses a low pressure (LP) turbine stage towards the rear of the engine to drive the intake fan at the front of the engine. The Trent family of engines have high bypass ratios which results in approximately 80% of the engines total thrust being developed via the low pressure bypass flow, This does not pass through the compressor and turbines stages. Energy extracted from the core gas fuelled flow by the LP turbine stage still produces thrust but at lower velocities.

The reduced jet velocity has the advantage of significant noise reduction and lower fuel consumptions. This arrangement with multiple turbine stages yields twice the thrust of a turbojet for an equal core size. In addition, the turbofans offer significant noise reduction and lower fuel consumption rates whilst retaining sufficient thrust.

The turbofan bypass ratio allows for design versatility to suit different applications. Military turbofan designs have a medium to low bypass ratio with less turbine stages which produce higher jet velocities. Low bypass ratios are preferable to maintain low airflow distortion at the inlet to maintain stable thrust availability during combat manoeuvres. Military afterburners mix and ignite fuel in the jet stream. The fuel-air mixture increases the exhaust temperature and subsequent velocity. The adjustable nozzle diameter combined with additional exhaust flow rates increase the aircrafts maximum thrust. Afterburners are only used in short durations because of the high fuel consumption levels required.

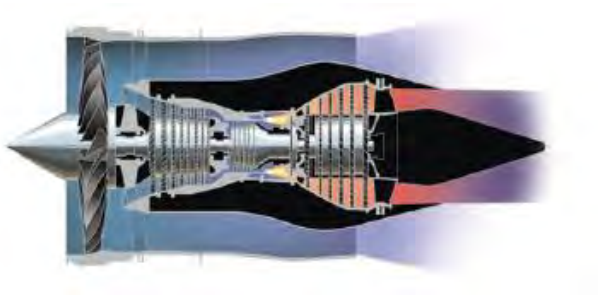

Figure 2-5. Modern turbofan schematic [1].

For the purpose of this work any reference to high pressure turbine discs or engines shall refer to the commercial Trent family or similar commercial turbofan designs, see Figure 2-6 unless otherwise stated.

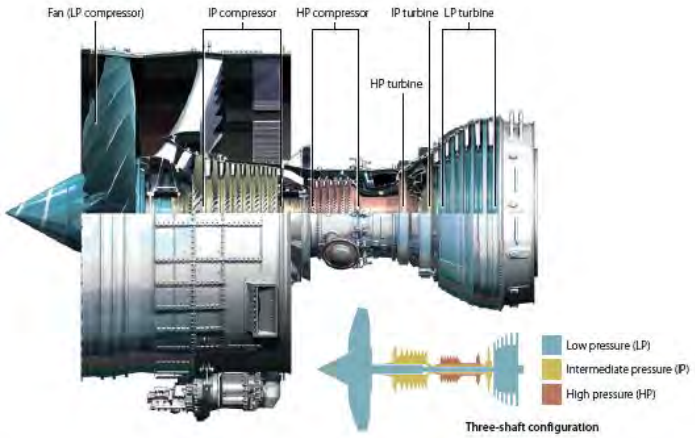

Figure 2-6. Trent high-bypass three-shaft turbofan design [1]

2.4 Aerospace Materials

Simple examples demonstrate the variety of materials used in a civil aerospace engine design. As discussed later, the turbine and compressor sections of the engine experience extreme temperatures. Nickel-base superalloys are used because of the mechanical property retention, amongst others factors, at high temperatures. The fan systems often uses titanium alloys like Ti 6-4 because they have good corrosion resistance and has a high specific strength which is important because of the fan blade size. To encase the fan blades one of the primary materials used in the casings are composite braids made from either carbon or aramid fibre reinforcements. These offer a significant weight saving overall. Finally, high performance steels are used

for shaft designs because of their torsional strength and thermal characteristics.

2.5 High Pressure Turbine Discs

The HPTD is considered to be a critical component by manufacturers. This means failure can result in significant hazard to the aircraft [1]. The primary purpose of the disc is to retain the turbine blades via fir-tree-root fixtures for example. The second purpose of the disc is to transfer torque, generated by the high pressure gas flow passing over the high pressure (HP) blades, to the central drive shaft. Therefore, disc alloys are generally designed according to the following key requirements:

(i) High operating temperature capability, typically in excess of 650°C at the disc rim.

(ii) High UTS and proof stress to withstand centrifugal loads to prevent fracture and yielding.

(iii) Fatigue resistance and low creep rates. Although, stress relaxation can be beneficial locally around stress raisers.

(iv) Ductility and fracture toughness are required to compensate for defects and damage which are critical for the purpose of this project.

The dominant requirements vary across the cross-section of the disc. The rim and bore of the turbine disc experience different operating conditions in terms of temperature and applied stress. The disc rim can be

exposed to temperatures in the region of 700°C and stress of ~ 300MPa. The alloy therefore requires a low creep rate which ideally suits a coarse grained microstructure. In contrast, the temperatures at the disc bore are lower, around 400°C. However, due to disc rotational speeds of 12,000 rpm the operating stress can exceed 1000 MPa which favours a fine grained structure [2, 3]. Currently, in-service alloys optimise grain microstructure to balance disc alloy requirements. The trade-offs that alloy designers are forced to make has driven developments of dual microstructure discs as a potential solution. These are created using variable heat treatments in the radial direction of the casting blank to create a differing grain structures across the disc cross-section [4].

Chapter 3:

Superalloys

3.1 Superalloy Development

High temperature components within aerospace engines have been dominated by nickel-base superalloys since the early 1940's. This is due to their ability to retain integrity under loading at operating temperatures close to melting point combined with good creep stain resistance. This is largely due to the face-centred-cubic (FCC) structure of nickel which provides both tough and ductile properties due to electron bonding energy [5]. No phase transformations occur from room temperature up to melting point eliminating any volumetric changes at high temperatures. Finally, the diffusivity of nickel at temperatures approaching melting point is low which results in a low creep rate [5]. Nickel-based superalloys also perform well

against corrosive substances such as salt water, potassium which can be found in aerospace and land based applications' salts and sulphur fumes during coal-fired electricity generation [5].

3.2 Manufacturing Developments

There have been three major manufacturing progressions since the original wrought alloys which dominated form ~ 1940 – 1960. The progression to cast alloys firstly improved the creep performance coupled with advances in vacuum induction casting of the 1950's which reduced the alloy impurity content [5]. An advance in casting techniques throughout the 1960's resulted in directional solidification developments by 1970. This technique only allows crystals with certain orientations to enter the casting. This reduces transverse grain boundaries which are susceptible to creep and form columnar structure [6]. The final step was to eliminate grain boundaries altogether which began in the 1980's[5], see Figure 3-1. This allowed for the removal of grain boundary strengthening elements which facilitates better heat treatment processes to improve fatigue life [5, 7].

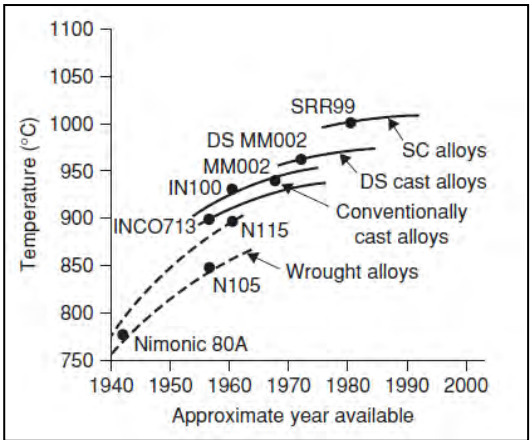

Figure 3-1. Nickel based disc alloy design and development timeline [8].

3.2.1 Ingot Metallurgy

Ingot metallurgy refers to the conventional cast and wrought processes. Turbine discs are manufactured via this route currently, typically in Waspaloy and IN718 polycrystalline alloys [8]. The basic process can be seen in Figure 3-2 flowchart.

The choice to manufacture via an ingot route as opposed to others such as powder metallurgy (P/M) is driven by commercial and metallurgical factors. Lower levels of alloying elements generally don't require expensive processing techniques to avoid segregation [8]. Near net shapes can be formed and any waste can be re-melted. This process can also be completed relatively quickly which when combined with other advantages results in a low cost process [2, 5].

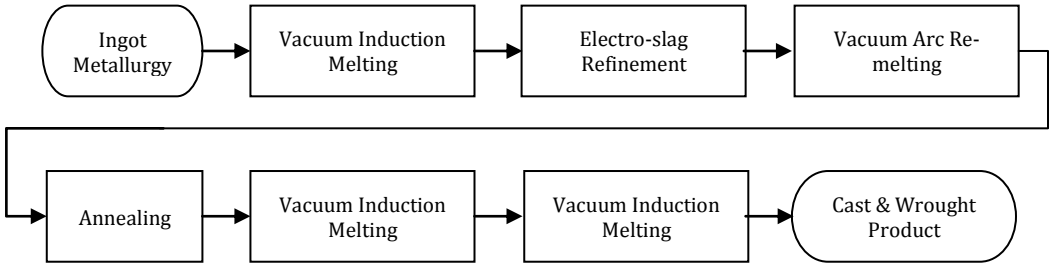

Figure 3-2. Basic cast and wrought processing route flow diagram.

Ingot metallurgy unfortunately suffers from inherent drawbacks due to the amorphous nature of the casting process which include segregation and porosity. Defect known as white-spots are solute lean regions which lack solid solution hardening elements. These lead to areas of reduced UTS and yield stress (σ_y). Another common defect is known as feckling which is

caused by alloying elements preferentially segregating to the interdendritic regions during the liquid state [5]. Certain parts of the process can cause localised temperature increases above solvus causing accelerated grain growth and inconsistencies. Other inconsistencies can arise from the introduction of defects during the process such as oxides and carbides due to the lack of microstructural control.

3.2.2 Powder Metallurgy

For higher alloying element levels in superalloys such as RR1000, required for more demanding operating conditions, P/M routes are used to avoid inhomogeneous microstructure and phases which cause segregation and cracking under extensive mechanical working stages. Consequently the P/M process is more time consuming and complication which ultimately leads to higher costs.

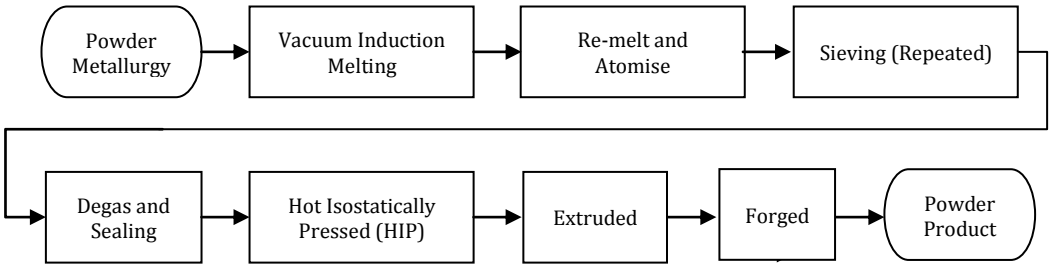

Figure 3-3. Basic powder metallurgy processing route flow diagram.

The sieving stage in Figure 3-3 is vital to ensure purity from defects which can be introduced during atomising shearing refractory particles which could be mixed into the melt. Another method to avoid contamination is the use of argon gas, which is inert, as the atomising agent.

The P/M process has many advantages such as grain size control, uniformity, a segregation free microstructure and an ability to undergo high temperature working processes [9]. P/M processes have high densification - approaching that of the parent material. This allows for close to net shape forgings with complex geometries to be achieved.

This manufacturing technique has a monetary drawback which is driven by the additional processes, the continual quality checks at each stage and the respective time scales attached to each [2]. Unfortunately these steps and precautions are imperative as small inclusions can dramatically reduce a components fatigue life.

3.3 Superalloy Composition

The chemical composition of a Ni-base superalloys is extremely complex, often including ten individual alloying element from a possible nineteen different alloying elements historically used in commercial superalloys. Examples of common compositions of cast and wrought alloys and the benefit of each alloy can be seen in Table 1.

Alloys such as IN718 contain similar proportions of Fe compared to Ni and hence should be known as Nickel-Iron Superalloys but shall be referred to as a nickel-base superalloy hereafter.

3.4 Superalloy Physical Metallurgy

The ability of superalloys to operate at high temperatures and to retaining high strength is due to microstructural hardening mechanisms.

Solid-solution and precipitate hardening can significantly increase the strength of superalloys by inhibiting the dominant microstructural deformation mechanism, dislocation motion.

3.4.1 Solid-Solution Hardening

Solid solution strengthening mechanisms inhibit dislocation motion in various ways depending on the solute atoms interaction with the solvent matrix. The local modulus within a given grain can be modified with the addition of solute alloying atoms of varying size and random distribution. These create strain variations due to the tensile or compressive stresses applied to the solvent parent matrix. The atomic size difference disrupts the slip planes creating resistance to the dislocation motion. An increased external stress is then required to provide the required energy for dislocation motion to occur in these areas [2, 10]. Creep resistance has been shown to improve with increases in solute alloying element weight percentage. A strong relationship has also been established between the creep strength of a material and atomic size discrepancy between solute and nickel solvent atoms [5].

Table 1. Chemical composition and doping elements of common superalloys. Data from [5, 8]

Cast Alloy	Cr	Co	Mo	W	Al	Ti	Ta	Nb	Re	Ru	Hf	C	B	Zr	Ni
CMSX-4	6.5	9.6	0.6	6.4	5.6	1.0	6.7	-	3.0	-	0.1	-	-	-	Bal
Rene 125	9.0	10.0	2.0	7.0	1.4	2.5	3.8	-	-	-	0.05	0.11	0.017	0.05	Bal

Wrought Alloys	Cr	Co	Mo	W	Nb	Al	Ti	Ta	Fe	Hf	C	B	Zr	Ni
IN718	19.0	-	3.0	-	5.1	0.5	0.9	-	18.5	-	0.04	-	-	Bal
Rene 95	14.0	8.0	3.5	3.5	3.5	3.5	2.5	-	-	-	0.15	0.010	0.05	Bal
Udimet 720Li	16.0	15.0	3.0	1.25	-	2.5	5.0	-	-	-	0.025	0.018	0.05	Bal
RR1000	15	19	5	-	1	3	4	2	-	1	0.03	0.02	0.06	Bal
Wapaloy	19.5	13.5	4.3	-	-	1.3	3.0	-	-	-	0.08	0.006	-	Bal

Elemental Influence	Cr	Co	Mo	W	Nb	Al	Ti	Ta	Fe	Hf	C	B	Zr
Matrix Strengtheners	X	X	X	X									
Gamma Prime Formers					X	X	X	X					
Carbide Formers	X		X	X	X	X		X		X			
Grain Boundary Strengthening										X	X	X	X
Oxide Scale Formers	X					X							

Within a FCC crystalline structure the close packed planes are stacked in groups of three, i.e. ABCABCABC where A, B and C are close packed layers. The removal (intrinsic) or addition (extrinsic) of one or more of these layers creates a stacking fault which changes part of the crystalline structure from FCC to HCP, denoted by ABABABAB. The addition of Co or Cr in superalloys, which can also be dissolved in ɣ', increases the ɣ' solvus and lowers the stacking fault energy [11]. This makes it more difficult for dislocations to move onto new planes which prevents creep [12].

3.4.2 Precipitation Hardening

Precipitation hardening describes the dispersion of strong particles which impede dislocation motion to prevent creep [13], see Figure 3-4. In nickel-base superalloys ɣ' particles form an ordered FCC crystalline structure similar to the ɣ matrix phase. The properties of these alloys are highly dependent on the ɣ/ɣ' interfacial strength. Other precipitates include the gamma double prime (ɣ''), topologically close-packed (TCP) phase, and the carbide and boride phases which precipitate on grain boundaries.

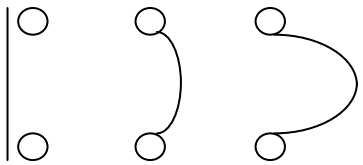

Figure 3-4. Example dislocation motion (left to right) around precipitates.

3.4.3 Volume Fraction

Gamma prime precipitation formation and growth can be controlled by heat treatment and high temperature cycling. Above a ɣ' volume fraction of 60% the alloy ductility will be compromised becoming increasingly brittle as the percentage volume increase [14].

The term volume fraction describes combined volume of primary, secondary and tertiary ɣ'. The optimal fraction of each type must be achieved within the microstructure to provide maximum alloy strength, creep resistance and fatigue life. The nucleation and growth of all three differ depending on initial heating and aging.

(i) Primary ɣ' – formed of the remaining ɣ' molecules that do not enter solution and caused by solutioning temperatures below the required solvus temperature. Primary ɣ' resides at the ɣ-phase boundaries preventing grain growth [15].

(ii) Secondary ɣ' – exists in solution within the ɣ grains formed at high temperatures when cooled from above the solvus temperature. Cooling rate determines the secondary gamma prime size which is typically within the diameter range of 70-120 nm [2, 15].

(iii) Tertiary ɣ' – further precipitation at lower temperatures form tertiary ɣ'. This can also occur due to quenching and ageing, the relative diameters are between 5-10 nm. Tertiary ɣ' has been show to coarsen during aging, growing to a larger range of 15-50 nm [2, 15].

3.4.4 Gamma Phase

The nickel base element forms a continuous FCC matrix known as the gamma phase (ɣ). Due to their position in the periodic table in relation to Ni elements such as Cobalt (Co), Chromium (Cr), Molybdenum (Mo), Ruthenium (Ru), Rhenium (Re) and Tungsten (W) inherently partition to the ɣ matrix phase. Substitutional solid solution strengthening can occur between elements of similar size (± 15% volume) by replacing the parent atom with minimal lattice distortions [2], this has a stabilising effect on the ɣ phase. Elements such as Cr (+3 vol.%), Mo (+12 vol.%) and W (+13 vol.%) are example of common substitutional elements. Interstitial atoms inhabit voids between the parent matrix, creating lattice strain. Boron (-21 vol.%) and Carbon(-27 vol.%) are amongst the few elements which are small enough amongst the alloying elements [5]. A pictographic representation of both substitutional and interstitial atoms in solution is shown in Figure 3-5.

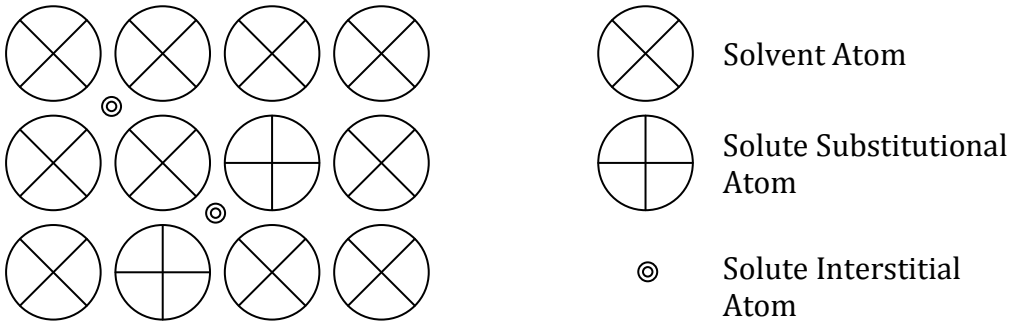

Figure 3-5. Solid solution representation (Not to scale).

3.4.5 Gamma Prime Phase

The strength of nickel-base superalloys is derived from the formation and dispersal of the gamma prime (ɣ') precipitates. The gamma prime phase consists of nickel combined with aluminium, tantalum or titanium to form compound precipitates, Ni_3Al, Ni_3Ta or Ni_3Ti respectively. The crystalline structure of ɣ' is a primitive cubic $L1_2$ structure similar to the ɣ matrix which creates stability, see Figure 3-6.

The strength of the ɣ' phase is associated with extensive directional covalent bonds and preferential Ni-Al bonding due to the respective crystalline structures [5]. This results in a strong chemically ordered

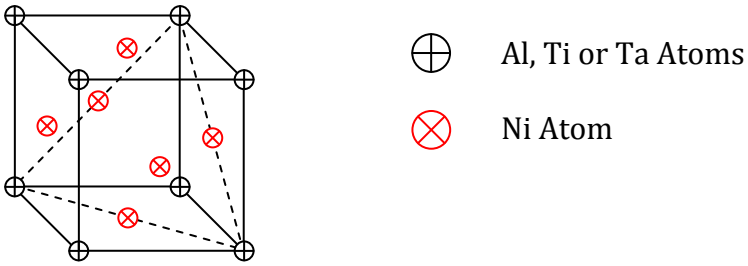

Figure 3-6. Primitive cubic $L1_2$ gamma prime unit cell.

structure. The presence of gamma prime can be identified through transmission electron microscopy (TEM) analysis and characterised by a cubic structure which develops from spherical precipitates during aging [16].

3.4.6 Gamma Double Prime

In alloys such as IN718, which contain a high proportion of Fe and Nb the gamma double prime (ɣ'') phase is the dominant precipitate. This phase exhibits a body centred tetragonal (BCT) the $D0_{22}$ crystalline ordered nickel-niobium intermetallic compound structure Ni_3Nb. The ɣ'' precipitates are

characterised by a spherical disc morphology. The $D0_{22}$ structure of ɣ'' has very few slip planes which make it ideal for polycrystalline high temperature applications such a turbine discs [17].

However, at temperature approaching 700°C the orthorhombic delta phase (δ) forms, which does not increase strength and nucleates along ɣ grain boundaries, instead of the strengthening ɣ'' phase. Above 700°C rapid coarsening of ɣ'' is observed until 850°C when ɣ'' becomes unstable and δ phase forms rapidly [5]. When controlled carefully the δ phase is desirable for grain size control and stress rupture ductility [18].

3.4.7 TCP Phases

Intermetallic TCP phases are detrimental to mechanical properties of superalloys. These phases form at grain boundaries where solid-solution element concentrations are highest. Two common TCP phases are sigma (σ) and mu (μ) which comprise of element including Fe, Ni, Cr, Co, Mo, W and Re. In general Ni, Cr and Fe occur in the σ phase and W, Mo and Co form in the μ phase. This is determined by elemental electro-negativity [5, 19]. Careful control of these alloying elements is required to avoid nucleation of these phases.

Areas of depleted solution strengtheners soften the ɣ matrix creating areas of localised strain variation which affects creep rupture properties. The TCP phases can be characterised by dendritic needle-like, platelet or blocky structures [2].

3.4.8 Borides and Carbides

Borides are created when surplus boron combines with elements such as Ni, Cr, Mo and Ti. The M_3B_2 borides reside at the grain boundaries, no negative effect of boride formation has been observed. However, boron and boride migration at the grain boundaries may cause a pinning effect which impedes grain growth.

Similarly, carbides also form preferentially at grain boundaries combining carbon and Ni, Cr, Mo and Ti. Other carbide forming elements include Hf, Nb, Ta and V. The effect carbides have on superalloys is more complex as they are both advantageous and disadvantageous depending on the type of carbide formed and governed by high treatment [9]. Carbides are also found at interdendritic regions and have been suggested to initiate TCP phases [19]. The four basic type of carbide[1] are described below [2, 5, 9, 10, 20]:

(i) MC – This carbide forms first after solidification at grain boundaries and within the matrix. They display a cubic appearance and are distributed heterogeneously within the FCC structure. At low temperatures ductility is improved whilst at high temperatures creep resistance is increased.

(ii) M_7C_3–These are less common but present superalloys such as Nimonic 80A when heated above 1000°C. The general shape is

[1]Where M is the metal alloy atom, i.e. Ni, Cr, Hf, Mo, Nb, Ta, Ti or V, and C is carbon.

blocky and precipitation takes place at the grain boundaries. They have a beneficial effect in small discrete occurrences but detrimental if they form a grain boundary film.

(iii) $M_{23}C_6$ – Formation of these carbides happens at low temperature or in-service (500 - 850°C). The particle inhibits grain boundary sliding. The complex cubic structure is similar to TCP σ phase which is why the two are related in terms of localised synergistic formation incidences. As with M_6C ductility can be compromised due to grain boundary embrittlement, fracture or de-bond from the carbide-matrix interfaces.

(iv) M_6C – Have similar mechanical properties to $M_{23}C_6$ but remain stable at higher a temperature which is important for grain size control. Conversely they also reduce ductility. Visually, they exhibit a blocky and occasionally Widmanstatten morphology. The carbides form when Mo and/or W content exceeds 6-8 at.% at a temperature range of 815 to 980°C.

It is now accepted that carbides and borides improve creep properties at high temperature. They have been found to increase rupture strength by precipitating at grain boundaries and reducing grain boundary sliding. Due to the nature of carbon and boron they exist at the ɣ grain boundaries. Carbides and borides are more common in polycrystalline alloys [5, 9].

Chapter 4:

Fatigue

4.1 Introduction

One of the most common modes of failure in metallic components is fatigue. Fatigue describes the cumulative structural degradation of a component under cyclic loading over time. Metal fatigue usually consists of metallurgical and mechanical factors such as material microstructure and damage cycles.

4.2 Fracture Mechanics

Fracture mechanics are applied throughout engineering to form initial mechanical fatigue crack initiation and propagation analyses. Any microstructural and compositional conditions are not taken into account at

this initial point. At this stage materials are assumed to be linearly elastic and homogeneous.

One of the fundamental relationships describes the linear elastic portion of the crack growth against stress intensity curve is known as the Paris Law (3)

$$\frac{da}{dN} = C\Delta K^{m} \tag{3}$$

Another basic fatigue damage relationship uses Miner's rule (4), which assumes the principal of superpositions. Damage is considered to be caused by individual loading-unloading cycles and is accumulated linearly to represent total damage. Other factors such as residual stress and plasticity contribute towards the inaccuracy of this approach.

$$\sum_{i-1}^{k} \frac{n_i}{N_i} = C \tag{4}$$

Some components do not operate solely within the elastic regime and therefore plastic strain needs to be incorporated. Basquin's Law (5) is used to assess the elastic-plastic cyclic deformation in terms of true stress and true strain.

$$\frac{\Delta\sigma_{true}}{2} = \sigma_f' \left(2N_f\right)^{b} \tag{5}$$

The term $\sigma_{true}/2$ is elastic-plastic strain amplitude, N_f is number of cycles to failure, σ_f' is fatigue strength coefficient and b is the fatigue strength

exponent. Fatigue calculations in real engineering structures require additional factors including mean stress effects, plasticity and stress concentrations discussed later. Factors of safety and worst case scenarios are used to validate these assumptions for complex real world applications.

4.2.1 Fatigue Crack Modes

Through thickness straight crack or elliptical edge cracks at the maximum depth are often used with empirically developed mathematical solutions used to calculate crack propagation. Three operating modes which describe crack propagation that are commonly used and are shown pictographically in Figure 4-1.

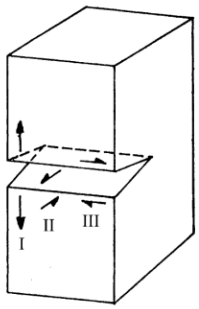

Figure 4-1. Crack opening modes diagram [21]

(i) Mode I (Crack Opening) – Opposing external tensile stresses act on planes in order to open the crack parallel to the crack surfaces. This is the mode which will be applied throughout testing as part of this work.

(ii) Mode II (Edge Sliding) – Shear stress encourages fracture surfaces to move across each other perpendicular to the crack through thickness edge surface.

(iii) Mode III (Shear Tearing) – Shear stresses operate parallel to the crack depth plane.

4.2.2 Ductile Fracture

Nickel-base superalloys incorporate strengthening precipitates such as gamma prime, gamma double prime, borides and carbides which serve as inhibitors but can also be sources of initiation due to localised stress imbalance causing stress concentrations or in excessive amounts an increased global brittleness. These are called secondary phase particles and can give rise to micro-void formation when a strain is applied. Failure stems from decohesion from the matrix leading to ductile fracture, see Figure 4-2.

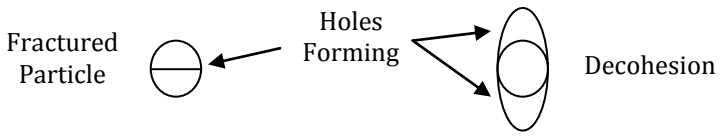

Figure 4-2. Basic ductile fracture mechanisms

4.2.3 Brittle Fracture

Brittle fractures occur very rapidly with little warning in engineering structures. These can be characterised as both intergranular and transgranular in morphology. In general, brittle fractures propagate according to crystallographic plane orientation with transgranular morphology and are also called cleavage events. They occur in FCC nickel-base superalloys under aggressive environments and high peak stresses. Typical examples can be seen in Figure 4-3.

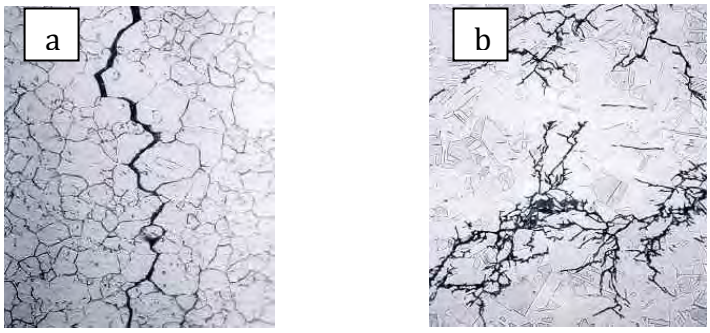

Figure 4-3. Fracture patterns, intergranular (a) and transgranular morphologies (b) [22]

4.2.4 Fatigue Fracture

The predominant damage mechanism for disc components is low cycle fatigue (LCF) failures. As discussed above, fatigue is the cumulative cyclic strain of a material characterised by plastic deformation. Traditional approaches use the Paris Law and others including Basquin and Miner Law. The most common representation of fatigue lives are S/N curves, see Figure 4-4. These will be used throughout this work to represent fatigue test data.

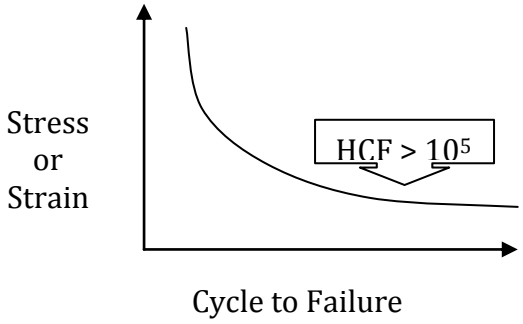

Figure 4-4. Typical S/N curve representation.

4.2.5 Crack Initiation

Fatigue mechanisms alone rarely apply to superalloys as their applications are high temperature and environmentally aggressive. Fatigue crack initiation can be caused by many different mechanisms. One such

mechanism is at persistent slip bands (PSB). Extrusion and intrusions at PSB act as stress concentrations, the misfit between the ductile plastic zone and the brittle matrix interface can also be a source of crack initiation. Other sources of initiation include twinning boundaries, carbides/boride inclusions and pores [23]. An important factor during small crack growth is grain size as boundaries act as inhibitors to the preferential 45° high shear stress planes which stage I cracks often propagate along. Under or over-aging has been shown to reduce early initiation due to the homogenised slip distribution in superalloys [24]. Other influences such as oxidation assisted cracking have been suggested as contributors to stress concentration points.

4.2.6 Crack Propagation

Crack propagation describes the steady-state crack growth through a component and the fast growth to failure. Fatigue crack propagation in a material is dependent on applied load, stress concentration factor, temperature, environment and geometry. Assuming the plastic zone ahead of the crack tip remains sufficiently small in comparison to the bulk geometry crack growth will remain linearly elastic. Increasing grain size is the primary method of increasing cyclic crack growth resistance and has been seen to reduce transgranular crack growth rates in some superalloys [24].

4.2.7 Stress Concentration Factors

In order for a crack to propagate the stress intensity factor, denoted by 'K', must exceed the materials fracture toughness, K_c, where *c* indicates

critical values at fracture. In descriptive terms K represents the local stress field or driving force at the crack tip.

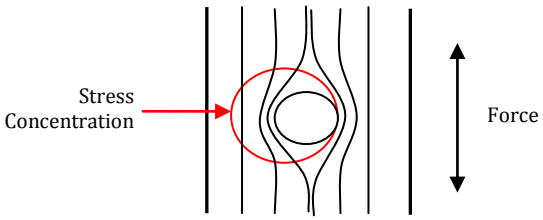

Figure 4-5. Stress contours in the presence of a defect of hole.

Small radii or holes cause increased localised stress concentrations. These produce a disturbance of internal stress states. Contours of stress can be used to describe stress concentrations, shown in Figure 4-5. Stress contours in the presence of a defect of hole. Peak stress occurs at θ = 90 and -90, where θ = 0 is parallel to the applied force. The K_t factor is calculated by dividing the local maximum stress at the concentration location by the global applied stress.

Additionally, the increased tensile stress created by stress raisers features such as holes and fir-tree root fixture radii on turbine discs creates a perpendicular and tangential stress state. The following set of equations (6) can be used to determine the stress components,

$$\begin{aligned}
\sigma_r &= \frac{\sigma}{2}\left(1-\frac{a^2}{r^2}\right)+\frac{\sigma}{2}\left(1+\frac{3a^4}{r^4}-\frac{4a^2}{r^2}\right)\cos 2\theta \\
\sigma_\theta &= \frac{\sigma}{2}\left(1+\frac{a^2}{r^2}\right)-\frac{\sigma}{2}\left(1+\frac{3a^4}{r^4}\right)\cos 2\theta \\
\tau &= -\frac{\sigma}{2}\left(1-\frac{3a^4}{r^4}+\frac{2a^2}{r^2}\right)\cos 2\theta
\end{aligned} \tag{6}$$

4.2.8 Fracture Toughness

The above applies to two dimensional Modes I or II crack opening, where '*Y*' is a geometrical correction factor, '*σ*' is the applied stress and '*a*' is the crack depth in a centre crack specimen. Similarly, to calculate critical fracture toughness values are substituted into (7). Multiple variations of this equation exist which correlate to different geometries. In a three dimensional situation, which includes Mode III cracking, then the geometrical correction factor '*Y*' in (7) is replaced by 2/π for example, shown in equation.

$$K_{(I,II)} = Y\sigma\sqrt{\pi.a} \tag{7}$$

$$K_{(I,II,III)} = 2\sigma\sqrt{\frac{a}{\pi}} \tag{8}$$

Materials are most commonly defined in standard tests in terms of their plane-strain fracture toughness, K_{Ic}. This is regarded as a material constant and represents the minimum value of K_c for Mode I opening when the specimen thickness is at least $2.5*(K_I/\sigma_y)^2$. Below this thickness the plastic zone can allow yielding along the 45° planes and is therefore known as plane-stress fracture toughness [21].

A small difference exists between the physical and effective crack length which is caused by localised yielding at the crack tip [21]. The radius of a given plastic zone (r_y) can be calculated according to (9) and (10). When examining the metallurgical response on a microstructural scale these corrections may provide partial explanations.

$$r_y = \frac{1}{2\pi}\left(\frac{K_I}{\sigma_y}\right)^2 \text{ (Plane Stress)} \quad (9)$$

$$r_y = \frac{1}{6\pi}\left(\frac{K_I}{\sigma_y}\right)^2 \text{ (Plane Strain)} \quad (10)$$

Traditional fracture mechanics are not valid within the core region of the crack tip with a radius significantly less than $a/10$ due to non-linear effects of plasticity and other including non-uniform microstructures, residual stresses, surface conditions and micro-pores [21]. Due to the microstructural importance, residual stress and surface conditions analysed as part of this work render the traditional approaches invalid.

4.3 Fatigue Mechanism

The mechanisms of fatigue damage on bulk material is in the form of plastic deformation and dislocation movement caused by applied cyclic stresses below the yield stress. The majority of mechanical failures are attributed to fatigue. As fatigue cracks are often surface nucleated surface hardening is often used as a preventative step, known as shot peening.

Generally, fatigue has been empirically discussed in terms of low cycle (LCF), high cycle (HCF) and thermo-mechanical fatigue (TMF). All three of these classifications of fatigue can further be broken down into distinct phases in brittle materials as follows:

(i) Micro-structural changes.

(ii) Micro-crack initiations.

(iii) Coalescence of initiations and subsequent growth into macro-cracks (stage I crack growth).

(iv) Stable propagation (stage II crack growth).

(v) Fast fracture failure (stage III crack growth).

Cyclic fatigue of superalloys are governed by the interactions of dislocations with strengthening precipitates ɣ' and ɣ". Ni-base alloys demonstrate both cyclic softening and hardening. Cyclic hardening is brief and followed by continual softening except at high temperature when softening begins instantly [24].

4.3.1 Low Cycle Fatigue

Low cycle fatigue in specimens or component is characterised as fewer than 10^5 cycles. LCF stresses will often exceed the yield stress but remain lower than the UTS. This explains why the fatigue mechanism operates within the plastic regime. Common data that are produced for LCF are stress-life curves also known as S/N curves which plot stress amplitude and number of cycles to failure. The stress-life relationship is governed by the Coffin-Manson relation, see (11).

$$\frac{\Delta\varepsilon_P}{2} = C(N_f)^c \tag{11}$$

where, ε_p = plastic strain amplitude.

N_f = number of cycles to failure.

C = fracture ductility coefficient.

c = fracture ductility exponent.

Many fatigue estimations exclude real-world influencing factors such as plasticity at the crack tip, imperfection in the bulk material which are assumed to be perfectly elastic, and the implications of varying duty cycles. The latter is dealt with according to Miners Law, (12) and assumes the principle of superposition. This implies that the damage from each cycle amplitude is independent.

$$\sum_{n=1}^{n=i} = Ni(Ai) / Ni(Ai) \tag{12}$$

In relation to turbine disc applications the effect of high temperature has to be considered along with duty cycles and dwell times. Time dependent interactions such as creep and oxidation are also responsible for decreased fatigue life at higher temperatures.

4.3.2 High Cycle Fatigue

The term high cycle fatigue is generally used for cycle times which exceeds 10^5. Typical S/N curve data are gathered and collected according to Basquin's law, see (13). Many materials also experience a fatigue endurance limit.

$$\Delta\sigma.N_f^b = C \tag{13}$$

where, Δσ = stress range.

N_f = number of cycles to failure.

C = empirical constant.

b = empirical constant.

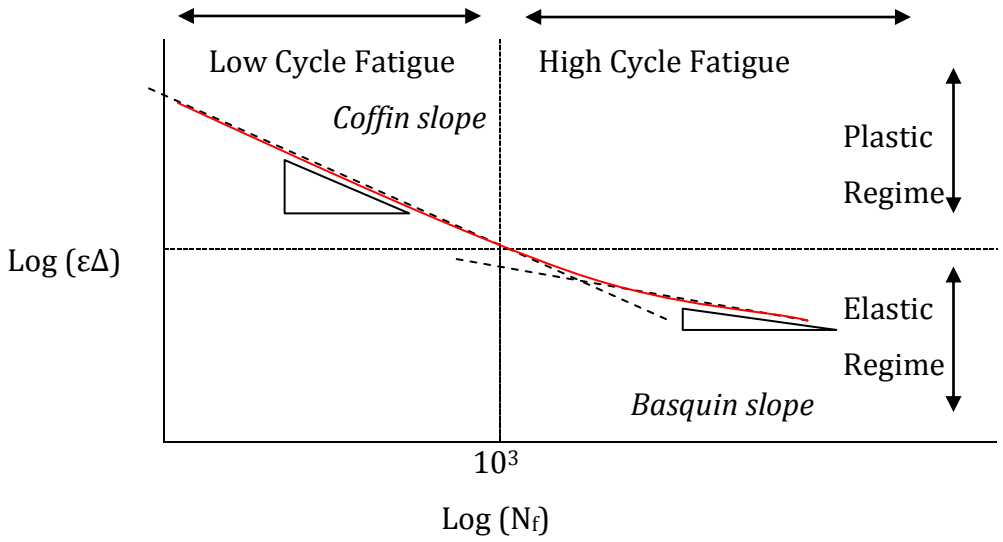

Figure 4-6. Cyclic fatigue regime classifications and governing equations.

In a gas turbine engine the HCF effects the turbine blades due to the vibrations that are produced by the gas flow over the aerofoil which imply a dependence on the R-ratio. Consequently, the single crystal structure of modern turbine blades make the orientation of the applied force in relation to the crystal orientation significant [5]. As $R \rightarrow 1$ the mechanism of failure is creep, as expected. It has been highlighted that at higher mean stresses, R = 0.1 and failure is again dependent of creep and can be shown in the fractographic post failure analysis. However, when R = -1 a cumulative fatigue mechanism has been observed, initiating within the material bulk from pores and brittle inclusions [5].

4.4 Fatigue Life

During this work the fatigue-life, design-life or simply the life of a components shall be taken to be the number of cycles required to initiate a

crack and propagate this crack until a critical length is reached, unless otherwise stated.

Theoretically, if design parameters such as yield strength, tensile strength and fatigue strength of a material are known during design a component which remains within the elastic regime at low temperatures can have an indefinite life. In reality other factors will prevent this such as wear and material defects. At high temperature deformation and fracture become time dependent due to creep phenomena and oxidation. Representative tests and lifing techniques are required to account for these variables.

4.4.1 Representative Testing

Full scale component testing can be extremely expensive and suffer from infeasible timescales. Also, components may fail under a number of non-fatigue related issues meaning components are often modified to encourage fatigue initiation in areas of interest. In addition, accurate fatigue predictions are heavily statistical which further increases cost and time to gain sufficient population distributions.

Pseudo testing of components range from scaled down assemblies to representative notched specimens. Uniaxial testing is commonly adopted for speed and cost reasons. These specimens can simulate stress concentration factors and surface conditions for example. Cost effectiveness allows large numbers of tests to be performed including factors such as dwell, overloads and environment. Other factors such as residual stress states and multi-axial

loading can be performed via modern numerical methods. During this work representative tests shall be used extensively for analysis and reference.

4.4.2 Analytical Techniques

Component failure in the life-to-first-crack (LTFC) or safe life method is defined as occurring when an engineering crack reaches a critical surface length. Spin rigs are used which replicate applied forces and operating temperatures. In turbine disc applications an engineering crack is 0.75mm which corresponds to the limit of non-destructive inspection (NDI) techniques. A safety factor is introduced by working to a design curve which is offset from the empirical life to failure against stress curve by minus three standard deviations (-3s.d.). This method is highly conservative resulting in approximately 99.9% of discs being retired with no surface crack initiation [3]. Additional data is also required for each material composition, surface condition, component geometry and operating environment. The additional testing required makes the safe-life approach too expensive. The approach also assumes materials are defect free which makes its approach limited when considering inclusions, pores and handling damage.

The Damage Tolerance technique assumes an initial flaw or defect always exists within the component which at minimum is the lower bound of detectable NDT resolution. The remaining fatigue life is then calculated using traditional fracture mechanics based around stress concentration factors [25]. If inspection does not find any damage the component can return to service and all data can be used to dictate future maintenance cycles based

on the NDT limit. This method is also conservative in the respect that work done during crack initiation and small crack growth is not taken into account [5]. Rolls-Royce has developed a residual life approach called Equivalent Initial Flaw Size (EIFS) which reverse calculates the initial flaw size based on a known failure event and maintenance routine schedules. These results are then collated into a databank of results which again serves to inform maintenance cycles. This has the advantage of not being limited by NDT techniques which results in longer life predictions [26].

Finally, the Probabilistic Approach techniques are based upon experimental results from test specimens. Statistical extrapolation techniques are applied to produce life predictions. For example, crack initiation in turbine discs due to LCF in P/M alloys are generally associated with pores due to insufficient densification and ceramic inclusions such as Al_2O_3 or SiO_2. The presence of these inclusions at the surface is more detrimental than when embedded within specimen or component [5, 9]. This implies that components with smaller surface areas will demonstrate better LCF properties and hence require geometrical probabilistic approaches. Other risk based lifing approaches measure safety against economic maintenance cycles and other drivers. Statistical methods are applied such as Taylor series expansions, Mean Value estimation Methods (MVM), First Order Reliability Methods (FORM) and Monte Carlo numerical techniques in conjunction with mechanical testing [27].

Currently Rolls-Royce uses the Total Life Approach. This approach takes into account initiation and propagation experimental data and combines numerical techniques. The total life approach uses the Walker (14) relationship which condenses test data at different mean stresses onto a single S/N curve.

$$\varepsilon_w = \left(\frac{\sigma_{\max}}{E}\right)\left\{\frac{\Delta\varepsilon E}{\sigma_{\max}}\right\}^{w} K_s K_{sc} \qquad (14)$$

4.4.3 Prototype Testing

Full scale fatigue tests can be carried out if desired or if required by regulatory bodies. Depending on the component these can be performed as a final proving exercise or during the design phase. Testing is expensive and in the case of HP turbines discs the spin rig tests are not required by American aviation authorities. However, in the UK it is required as final certification.

The details of a suitable duty cycle are simulated by computer controlled hydraulic rigs for simulated testing. Multiple loading systems can be simulated in parallel to mimic what each component experiences. The prototype mechanical test outputs can be used as numerical inputs for simulations to predict whole engine responses. Prototype tests have the advantage of accurately simulating in-situ high temperatures, low vacuum environments and environmental interaction with specific geometries.

4.4.4 Numerical Modelling

The finite element method and computational modelling have been shown to accurately predict component responses [3]. Numerical modelling can be used to predict fatigue crack growth in plain specimens and complex multi-physics scratch damaged situations [28, 29]. Pre-existing internal residual stress states can also be assessed avoiding volumetric and other physical limitation to mechanical testing by using the FE method [30].

4.5 Environmental Effects

Mechanical strength is time dependent at high temperatures and fatigue life becomes dependent on the number of cycles and the time per cycle. At high frequencies crack growth becomes cycle-dependent, however at low frequencies and during dwell time-dependent environmental influences dominate [31]. At high temperatures metals plastically deform at stresses below the UTS and σ_{yeild} known as creep. The literature describes this process as both being dislocation and diffusion based [32] and can affect both initiation and propagation [24].

Primary creep is heavily dependent on stress concentration factor leading to high crack growth rate. Secondary creep is independent of stress concentration factor and largely steady-state. The final stage of creep leads to fracture and is rapid.

Tensile dwell is common in turbine duty cycles causing HPTD components to be highly susceptible to creep and environmental attack, such

as oxidation and corrosion. During initiation oxidation can cause crack tip blunting which reduces the driving force and crack growth rate. In polycrystalline materials such as Alloy 720Li used during this work initiation may be transgranular but as temperature increases and the elastic modulus decreases and propagation becomes intergranular [5]. However, in gamma prime strengthened alloys compressive dwell at high strain rates also has a significant negative effect on fatigue resistance [24].

At intermediate test temperatures stress corrosion cracking effects the cyclic crack growth at the grain boundaries. Interestingly, the grain size of an alloy has a greater effect on environmental crack growth kinetics than composition. Studies have shown that grain size is the dominant factor in environmental crack growth rate trials. Other contributing factors include volume fraction of primary gamma prime and size and amount of coherent gamma prime when considering short crack growth [23].

4.6 Surface Conditions

Surface defects are a source of fatigue crack initiation. Machining without polishing can result in stress concentrations comparable to sharp notches. It is advisable to limit the machining operation orientations perpendicular to the applied force where possible. Machining with worn or damaged cutting tools increase the level plastically deformed material dramatically [33]. Beneficial surface treatments such as peening processes alleviate these affects.

Chapter 5:

Damage Tolerance

5.1 Introduction

High pressure turbine discs are known as Critical Group A components. The failure of these components can result in serious hazard to the aircraft. The damage tolerance of these components in addition to fatigue limits of the undamaged material needs to be understood for safe operational use and extended component life.

Traditional fatigue life techniques introduce temperature and variable strain interactions to produce design curves which are used with a sensitivity of -3 s.d. (standard deviation) according to a log normal bell curve distribution.

Modern techniques in the UK have been developed to overcome the excessively conservative nature of these techniques. One such development, described elsewhere, is the effective initial flaw size (EIFS). This utilises plain specimens, pseudo and real component data with fracture mechanics to reverse calculate the initial flaw size from known failure events.

The mechanical testing described within this programme of work shall contribute to existing databases for advanced lifing correlation activities.

5.2 Damage Simulation

Previous work in the literature has been conducted to demonstrate the effects of artificial damage in IN718 [34]. Tests have been conducted at 300 and 600°C over a range of scratch depth ranging from 25 - 125μm. The γ'' strengthening mechanism and test temperatures are below that of the experiments described in this work. The IN718 alloy was precipitation hardening and aged resulting in a fine grain structure and average hardness of 504 HV0.3. This is similar to Alloy 720Li and hence comparable.

The IN718 tests showed no notable detriment to fatigue life at all scratch depths for 300°C. Initiation was actually caused away from the scratch site in these cases. A number of hypotheses for these observations were eliminated including misalignment of testing apparatus and localised concentrations of carbides, borides and TCP phases which have been noted to be detrimental in excessive amounts. In was concluded that high tensile surface residual stress developed due to machining combined with scratch

tip blunting and lower stress concentration factors caused the surface initiations. The surface tensile stresses at 600°C are relaxed creating a higher localised stress at the scratch site. The depths of scratches at the higher temperatures therefore demonstrate a negative effect on fatigue life.

This shows that the role of residual stress needs to be considered as a potentially influencing factor in further analyses. The depth of compressive shot peening, surface machining stress states and relaxations all need to be taken into account when analysing the effect of scratch depth.

Further work carried out on RR1000 [28] addressed the influence of shot peening on scratched specimens. Tests were performed with no scratches, 50μm and 100μm deep scratches with and without shot peening. In general, shot peening increases the fatigue life of specimens at all scratch depths. However, the effect of shot peening diminishes at greater depths, see

Figure 5-1. The most significant fatigue life increase was when no scratch was present, whilst at 100μm the advantage of shot peening is extremely low and scatter makes a definitive conclusion difficult.

Cracks were shown to develop from the root of the scratch, where the stress concentrations factor peaks, nucleating from multiple points to coalesce and form a shallow crack the length of the scratch which propagates to failure. Further examination revealed a transgranular morphology band from initiation. Heavy oxidation was observed which indicates early initiation.

The literature does not indicate the role of residual stress induced during the scratching process. The stress-state balance between the shot peened layer and the area around the damaged zone may influence crack total life. The maximum depths of scratches in the literature do not exceed the compressive shot peened layer region. Beyond this beneficial layer any residual stresses present due to the scratching process will have a direct influence on total life.

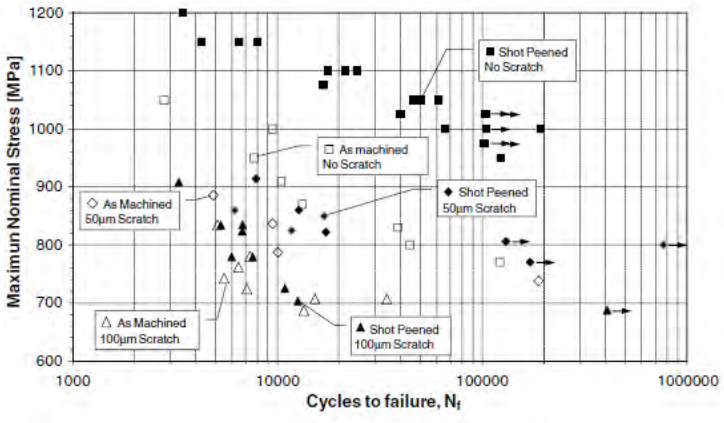

Figure 5-1. Uniaxial S-N data in the presence of artificial defects. [28]

Experimental results have also been successfully replicated numerically using FEM and the J-integral parameter. Once the initial high driving force of the transgranular morphology dissipates cracks have been shown to arrest at lower net stresses tested ~ 770MPa. FEM results correlate well with crack arrest limits defined experimentally for both machined surfaces and shot peened surfaces [28]. This indicates that numerical techniques can be successfully applied to simulate residual stress layers in Ni-base superalloys at high temperatures and in the presence of scratches.

This has the potential to be expanded to analyse the plastically deformed zone at the scratch tip root and the residual stress fields in the surrounding material caused during the scratching process.

Numerical and statistical techniques have been successfully applied to assess the role of microstructure on notched specimens. Artificial neural networks used by Pratt & Whitney to determine that for dwell cycles of 0 – 90 seconds a small microstructure performs better (~4 μm). The analysis included relaxation/creep resistance [35]. Conversely, at dwell times of 12,000 seconds a courser microstructure is favoured (~30 μm).

5.3 Preventative Techniques

The blending out of these scratch damage features has been show to bring fatigue life of a notched specimen back to that of a baseline notched specimen [36]. This is an option that manufacturers prefer as nickel components are extremely expensive and account for ~25% of the engine cost.

Further processes can be used which include additional shot peening and laser peening processes locally. However, these require additional maintenance and repair activities.

Chapter 6:

Residual Stress

6.1 Introduction

Residual stress can be defined as a tensile or compressive stress which acts on a bulk material independent of an external load. Residual stress is often characterised in respect to the scale they are measured to be acting across.

(i) Firstly, Type I residual stresses act on a macro-scale across several grains. This is typically the type which is referred to throughout the literature [34, 37].

(ii) Secondly, Type II residual stresses are often referred to as intergranular stresses as they show variation across individual

equal tensile stress over a larger region at a lower peak magnitude towards the centre of the bulk material. However, variations across the peened surface can exist due to shot angle of incidence especially around tight radii found at the dovetail fixtures for example [41]. Compressive residual stresses are beneficial for two reasons; firstly they retard crack initiation and propagation and secondly they reduce the high surface tensile stresses caused by machining.

Table 2. Measurement Techniques [38]

Measurement Method	Typical Application	Comments
Hole Drilling	Type I (in-plane)	Semi-destructive. Reduced sensitivity with depth.
Curvature	Type I (in-plane)	Must be performed incrementally. Destructive
X-ray Diffraction	Type I, (peak shifts)	Non-destructive surface technique.
Hard X-rays	Type I, II (peak widths) Type I, II (peak shifts) Type II, III (peak widths)	Small gauge volume.
Neutrons	Type I	Non-destructive. High cost and limited facilities available.
Ultrasonic	Type I, II, III	Microstructure sensitive. For magnetic materials only.
Ramen	TypeI, II	Non-destructive.

Claudio showed the relaxation of compressive residual stress profiles due to shot peening at temperatures of 650°C which are experienced in HPTD rims. At these temperatures the peak residuals are normalised [37]. Similarly,

grains. These occur in multi-phase materials due to thermal stress variations and surface textures [38, 39].

(iii) Finally, Type III residual stresses are considered to act on an atomic scale caused by chemical segregations at the grain boundaries causing dislocation stress fields for example [39, 40].

Residual stress interactions have been found to contribute to reduced component life in many applications including turbine discs for multiple different reasons. Residual stresses considered during this work shall predominantly be Type I.

6.2 Residual Stress Measurements

The commonly used techniques for residual stress measurement in bulk materials depends on the component for study, see summary in Table 2. The majority of experimental techniques cannot be performed during service or on large scale test pieces due to equipment limitations and the destructive nature of the processes. It is therefore important for residuals stresses to be understood and modelled throughout service-life to predict failure mechanisms occurrences.

6.3 Shot Peening

Shot peening is a process which bombards the surface of a metal with hard ceramic, glass or metallic balls to introduce micro-plasticity at the surface. This creates a surface compressive stress which is balanced by an

Evans showed that peak residual stress reduces by 50% in the loading direction during isothermal fatigue tests almost instantly within the first few fatigue cycles, see Figure 6-1 [37]. This suggests that this initial relaxation is temperature independent and caused by plastically deformed material. Evan further postulated that relaxation after 1000 cycles has been shown to be thermo-mechanically driven potentially via annihilation, creep and cyclic softening.

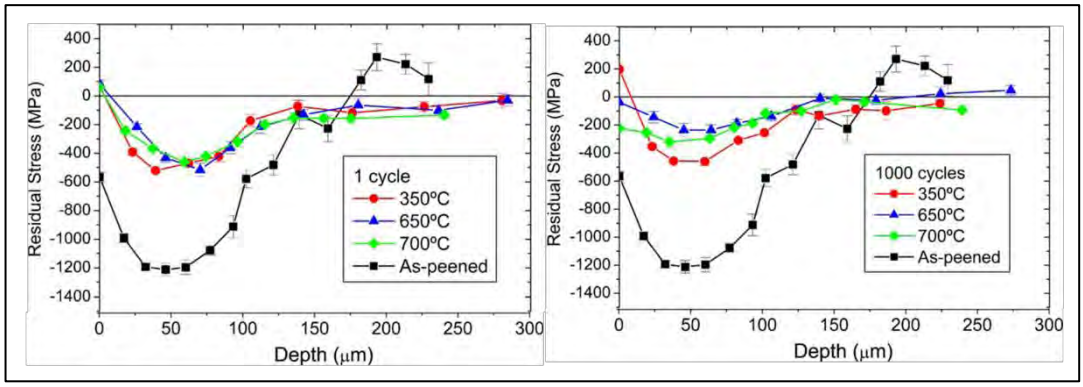

Figure 6-1. Residual Stress Relaxation at 1 Cycle (left) and 1000 Cycles (right)

6.4 Manufacturing

The machining parameters are important in real components. The selection of tools used has a significant impact on residual stresses and microhardness [42]. For example, Kwong et al [42, 43] tested two commonly used tools with different cutting edge designs and found that the residual stresses differ in both the radial and hoop directions. The magnitude and depth of the rhombic tool to introduces less work into the work piece. The most significant difference is displayed when a tool is broken or worn, plastic

deformation due to a broken tool has been shown to extend the work hardened zone to 300μm which is 5-8 times larger than the normal cases. The tool condition when producing artificially scratched specimens needs to be constantly checked to avoid similar consequences.

Surface roughness can create stress concentrations which can lead to crack initiations. Rough surface finishes can be caused by machining, such as turning operations and shot peening. These can lead to anomalous fatigue crack initiations away from predicted artificial scratch damage locations in certain tests [34]. This can be due to excessively high tensile residual surface stress which was found to be detrimental to fatigue life. Excessive shot peening can also create a rough surface that can create stress raisers.

The geometry of specimens can also effect the residual stress state, smaller specimens can misrepresent the actual components response and unloaded stress conditions. These stress-states can be further misrepresented when taking into account high temperature testing and thermal coefficients across non-representative material volumes.

Chapter 7:

Materials and Methodology

7.1 Introduction

In order to assess the safety of high pressure turbine discs (HPTD) manufacturers are required to demonstrate damage tolerance life capabilities to the European Aerospace Safety Agency (EASA).

In this thesis the type of damage analysed is associated to manual handling such as assembly and repair. Handling damage is the collective name for a variety of event resulting in small scratches on the surface of the component. These scratches can be caused during maintenance routines by dropping objects onto the disc for example. Alternatively, locating the tight fitting turbine blades into the disc at the fir-tree root fixtures can also cause small scratch surface damage.

The effects that handling damage has on the components microstructure and subsequent fatigue life are explored in this thesis using the techniques described below. All conclusions made from this assessment support the damage tolerance life of the Rolls-Royce Trent 900 HP Turbine Disc.

The following sub-chapter describe the techniques used to achieve greater understanding of the following:

i). Effect of scratch depth.

ii). Effect of single-pass vs. multi-pass damage simulation.

iii). Stress-states present.

iv). Implications of the above on fatigue life calculations.

7.2 Component Material

The alloy used in this study is Alloy 720Li, formally known as Udimet 720Li. This is a nickel-base superalloy developed by the Special Metals Corporation. Alloy 720Li (low inclusion chemistry) is derived from Udimet 720 with additional compositional differences show in Table 3.

Table 3. Nominal Alloy Composition [44]

Alloy	Cr	Co	Mo	W	Ti	Al	C	B	Zr	Ni
U720	18.0	14.7	3.0	1.25	5.0	2.5	0.035	0.033	0.03	Bal.
U720Li*	16.0	14.7	3.0	1.25	5.0	2.5	0.010	0.015	0.03	Bal.

*Alloy used for experimentation during this work

The 720 series of alloys are precipitation strengthened with γ' Ni_3 (Al, Ti) and solid solution strengthened with Cr, Co, Mo and W. They have been

designed to withstand oxidation and sulfurisation at high temperatures for specific application within the high pressure compressor and turbine sections.

Alloy 720Li features reduced proportions of C and B elements. Elongated carbide and boride inclusions which are often called stringers are produced. Stringer reduction produces a more homogenised microstructure during high temperature cast and wrought component manufacturing processes [44, 45]. Lower chromium content is applied to reduce the formation of the sigma phase. The σ phase is a topological close packed TCP structure which can form needle-like film at grain boundaries or form close to γ' and carbides. The σ phase depletes Cr from the γ matrix, which acts as a solid solution strengthening element [46].

Fatigue tests were by Rolls-Royce Plc on specimens taken from the three separate forgings described below.

A. Batch ID MER0044850 – specimens were extracted from an existing Trent 900, stage 6, HP compressor disc which has undergone full heat treatment for service entry condition.
B. Batch ID MER0044850 - DCPD calibrations specimens were extracted from a BR710, stage 1, HPTD forging.
C. Batch ID MER044987 – fatigue specimens were extracted from a BR710, stage 1, HPTD forging.

Forging A had an above average UTS value of +3.35 standard deviations from the population average which was measured from 201 manufactured forgings. Forgings B and C had below average UTS values when tested by Rolls-Royce. Forging B had a UTS of -0.64 s.d, whilst forging C was also -0.83 s.d. below their respective population averages. This is taken into consideration during results and discussion of the analyses.

7.3 Replica Scratches

A test plate was produced with a series of scratches using the single-pass and multi-pass methods at different depths, details of the methods can be found in 7.4.3. The scratches replicated are shown in Table 4. The test plate was not from the same forgings as the fatigue specimens but is produced to the same specification as production grade Alloy 720Li., as are the fatigue specimens. The test plate is also shot peened to the same specification as the fatigue specimens by Metal Improvement Company Ltd before being shipped to PS. Marsden Ltd for scratch creation.

The purpose of this test plate with replica scratches was to assess the effects on microstructure and hardness at varying depths of scratch and to also prove the damage simulation technique in alloy 720Li. This is intended to compliment fatigue life results during discussions.

Table 4. Replica scratch depth, scratching technique and number of scratches.

Scratch Depth (µm)	Scratching Technique
25.4	Single-pass (x 3)
50.8	Single-pass (x 3)
76.2	Single-pass (x 3) / Multi-pass (x 1)
101.6	Single-pass (x 3)
127.0	Single-pass (x 3) / Multi-pass (x 1)
254.0	Single-pass (x 3) / Multi-pass (x 1)

7.4 Fatigue Testing

A series of low cycle fatigue tests were completed at both Rolls-Royce and at the University of Birmingham designed to analyses the effects of temperature, dwell, scratching technique and total life and the proportion of time spent at initiation.

7.4.1 Uniaxial Tensile Specimens

Uniaxial tensile test pieces with different stress concentration factors of Kt1.1, Kt2.0 and Kt3.35 were utilised. The primary focus of this research adopts the Kt 1.1 geometries as, shown in Figure 7-1. Analysis shall be carried out on test results obtained from similar specimens with Kt2.0 and Kt3.35 notched geometries. The specimens were fly-cut at the notch location to best represent the 28m/min turning process subjected HPTD surfaces. A fly-cutting speed of 24m/min was found to produce an equivalent surface finish to disc components. The speed of cutting is important when

considering the microhardness of a components surface. Checks were performed to ensure minimal swept grains and sub-surface strain conformed to approximately 10 µm, as expected for HPTD surfaces. The Kt1.1 specimen geometry can be seen in Figure 7-1.

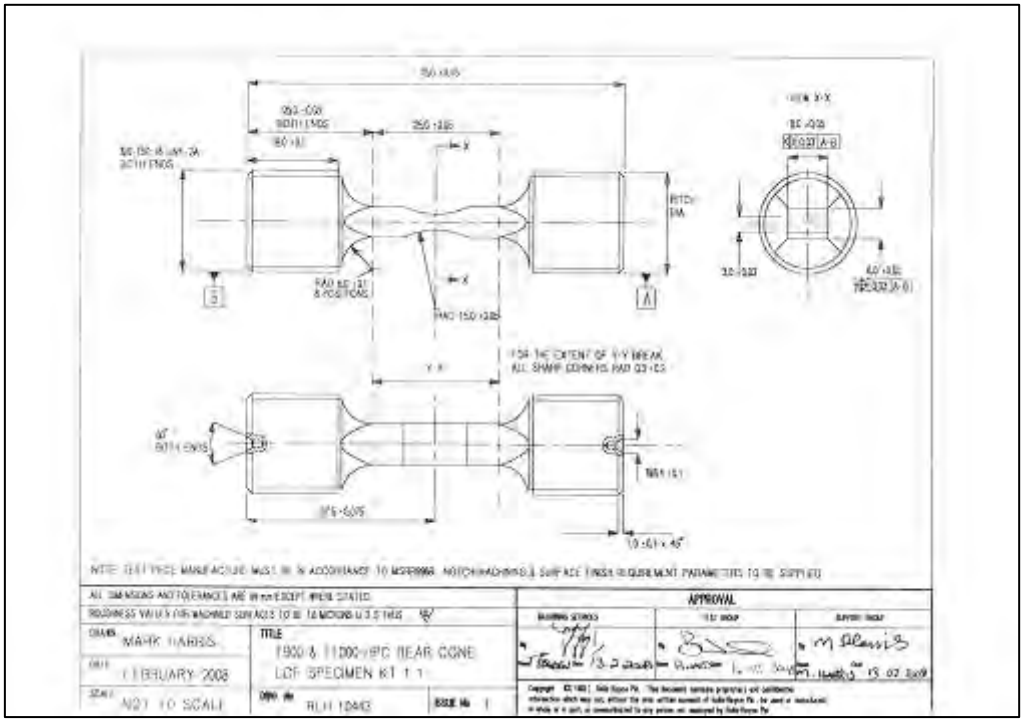

Figure 7-1. Engineering drawing of kt 1.1 notched uniaxial fatigue specimen.

7.4.2 Shot Peening

Prior to the scratching process all specimens were shot peened to the same specification as would be found on a HPTD finished component. The peening process was completed at Metal Improvement Company Ltd using the following parameters which are common for all critical parts.

i). 110H shot

ii). 200% coverage

iii). 6-8 Almen Intensity

7.4.3 Artificial Damage

To simulate the damage that has been found in real components an artificial technique was developed to compare damage in terms of penetrative depth. The Rolls-Royce developed precision scratching process was performed at P.S. Marsden Ltd, see Table 5 listed the basic scratch geometry. Firstly, the scratching process had to be proven in Alloy 720Li to show tooling was capable of producing the scratch in the harder alloy compared to IN718. The effects of material spring-back which may produce non-conformant scratch profiles was checked using a non-contact method.

Table 5. Geometric tolerances of artificially induced scratch damage.

	Feature Geometry	**Tolerance**
Scratch Length	3 mm	None stated
Scratch Profile Angle	90°	-2/+3°
Scratch Tip Radius	50 µm	-20/+30 µm
Overall Scratch Depth	12.7 µm 25.4 µm (+25.4 µm increments) 254 µm	None stated

Historically, limitation due to the tool rigidity relative to the hardness of Alloy 720Li made single-pass scratching processes difficult for high Kt factor specimens due to the geometrically slender tool requirements. For

continuity it was decided to use an iterative multi-pass technique. To achieve the desired depth each tool pass would remove 25.4 μm depth of material. For the maximum scratch depths up to 5 tools were used to ensure scratch tip conformity and avoid tool wear effects.

However, a new scratching technique has been developed which allows for single-pass processes to be used on all specimens. Analysis during this thesis shall consider the implications each technique has on microstructure and ultimately fatigue life.

The first tier of dimensional conformity checks were performed on all specimens to ensure scratch conformity to the values given in Table 5 by P.S. Marsden Ltd. The checks were performed using a dial test indicator and coordinate measuring machine. The second tier of checks were performed by Intertek using the non-contact confocal Alicona measuring system.

A fully prepared specimen ready for fatigue testing is shown in Figure 7-2. The specimen features a scratch in the centre of the notched face on each side oriented perpendicular to the applied force.

Figure 7-2. Untested, shot peened LCF specimen.

7.4.4 Low Cycle Fatigue Testing

Tests were carried out at a range of temperatures across the various Kt specimens. For the Kt 1.1 specimens the test temperatures were 600°C and 650°C, the later approaches the upper operating temperature that a HPTD experiences at the rim. The specimens were tested in an air environment which also makes them susceptible to oxidation effects.

The applied test load was defined based on peak elastic stress values calculated using the net section for each individual specimen. The maximum and minimum test loads were reduced as scratch depth increases because a lower net stress is required to yield similar life. A trapezoidal ramped waveform was used for all specimen tests, see Figure 7-3. The ramp input signal represents a linear ramp from the minimum load to maximum load in a period of 1 second. This is followed by a 1 second hold at maximum load followed by a 1 second linear ramp to minimum load and finally a 1 second minimum hold before repeating. In addition, a 60 second dwell cycles (1-60-1-1) has also been applied to the Kt 1.1 test matrix. The position of the 60 dwell within the 1-60-1-1 waveform indicates a hold at maximum load.

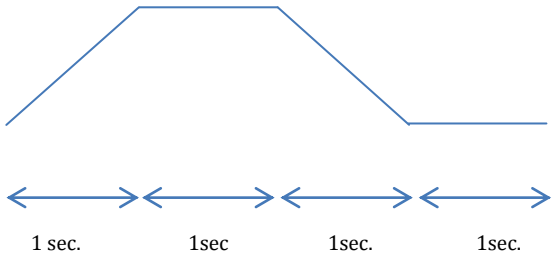

Figure 7-3. Trapezoidal Waveform

The testing performed at the University of Birmingham used an ESH Testing Ltd, servo-hydraulic test rig with computer control. The rig was equipped with a low flow valve which allowed for a high degree of accuracy to achieve the desired waveform.

7.4.5 Crack Growth Monitoring

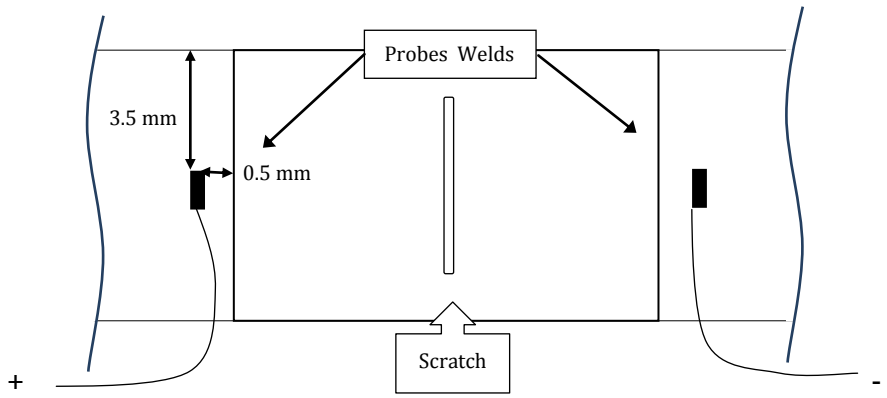

Figure 7-4. DCPD Probe Arrangement

Crack growth was monitored using the Direct Current Potential Drop (DCPD) technique at the University of Birmingham. Both cracks were monitored simultaneously using a twin channel chart monitor. Post-test analysis was performed to assess the cycles to initiation and the equivalent potential drop measured. The DCPD probe arrangement is shown in Figure 7-4.

Due to the long distance of the DCPD probes from the scratch site a high initial starting voltage of 6V was chosen which corresponds to previous Rolls-Royce tests. The power supplies used were operated under current

control. At test temperature a constant current of approximately 8.5 Amps is needed to achieve the 6 Volts initial voltage.

Beachmarking was carried out to assess the sensitivity of current settings to calibrate the P.D. and crack growth relationship. Beach-markings on the fracture surface were carried out by reducing the peak amplitude to 70% at a frequency of 0.25 Hz.. The test was switched to the original load amplitude after 1 μV increase in P.D. was observed. This technique successfully created a series of beachmarks on the fracture surface as shown in Figure 8-37.

7.5 Microhardness

Microhardness was used to assess the affected zone depths, which are compared to the measurements from optical microscope and SEM. The microhardness mapping was performed on scratches at several depths, various positions along the scratch and on both single-pass and multi-pass techniques. This may generate variations in elastic and/or plastic strains corresponding to the dynamic scratching process.

The microhardness equipment used was a Struers DuraScan which features an automatic focusing and measurement software systems called ecos-Workflow. Together with the computer controlled interface this allows a large number of test points to be analysed with a high degree of accuracy and confidence in a relatively short period of time compared to a conventional manual testing machine.

Specimens were cut and mounted in Bakelite and polished to a finish of 1μm before surface cleaning using ethanol. This produced a clean scratch-free surface which aids the automatic measurement system.

Due to the scale of the scratches and the level of granularity required a small indenter size was required, taking into account the necessary spacing for accurate measurement. A total of 293 hardness indents were performed over an approximate area of $1mm^2$. All indentations were pre-defined as Vickers HV0.1 according to EN ISO 18265. Hardness profile maps were output into MS excel file formats for post processing analysis in MATLAB.

7.6 Confocal

Confocal microscopes use a focussed beam of laser light to eliminate image noise from out of focus reflected light to gain a highly focussed image. A series of images can be captured moving through the z-axis and integrated together to form a three-dimensional map of the focussed portions of each image.

The confocal microscopes were used to firstly assess that all scratch profiles conformed to pre-defined specifications at Rolls-Royce. Further checks using confocal were completed at the University of Birmingham to evaluate the presences of residual stress based on the appearance of microhardness indents.

The measurement systems used were the Alicona InfiniteFocus Standard at Rolls-Royce and the Olympus Lext OLS 3100, with a TS-150 table stabilisation unit at the University of Birmingham.

7.7 Fractography & Metallography

Both optical and Scanning Electron Microscopy (SEM) images were captured to assess fracture surfaces and polished surfaces. SEM imaging was used to assess the visible grain deformation on the untested replica scratch specimens. ImageJ software was then used to measure the deformation zones in several locations. The deformation zone was first measured at the scratch root tip in three places around the radius to form an average. Further measurements were taken away from the root following the scratch surface towards the surface of the specimen.

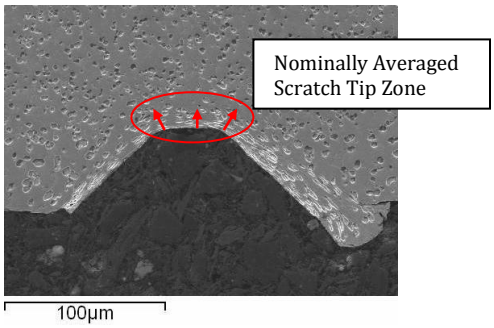

Figure 7-5. Diagrammatic representation of the averaging methods for a single nominal value for scratch root tip deformation depth.

SEM images of fracture surface morphologies in high magnification were also captured. These images were taken at the University of Birmingham, Centre for Electron Microscopy on the Joel 6060 conventional SEM.

Chapter 8:
Results and Discussion

8.1 Introduction

This chapter details the results obtained and analysed to fulfil the objectives of this thesis.

8.2 Alloy 720Li Damage Simulation

In efforts to reproduce handling damage experienced in-service and in some cases during manufacture a highly controlled and reproducible technique is required. Such a technique has already been established for multi-pass scratch damage creation. However, a refined single-pass method has recently been developed by P.S. Marsden Ltd and proven reliable in IN718. As this technique better represents the in-service damage process it was decided that all future research in this area use the new method where possible.

8.3 Geometrical Assessment of the Scratches

Initial checks were performed at Rolls-Royce using the non-contact Alicona InfiniteFocus measurement systems on replica scratches produced in a test plate, see Table 6. Measurements were taken in three positions equally spaced intervals along the longitudinal length of the scratch to identify any irregularities or differences between tool entry and tool exit interactions with the test plate. Averages were taken to nominally represent each scratch parameter with a single set of values , shown in Degree of Deformation

SEM and optical microscopes were used to examine the microstructural changes caused by the deformation process. The differences and trends were analysed in response to scratch depth, scratch creation technique and tool position, i.e. exit and entry deformation.

The increased hardness of Alloy 720Li and its elastic recovery characteristics have not diminished the ability of the scratching process to reproduce conforming scratch profiles at a range of depths using the single-pass technique. An over-check was performed at the University of Birmingham using the alternative Olympus LEXT systems which confirmed a selection of the Alicona measurements.

These geometric checks confirmed the single-pass technique was within tolerance for the harder Alloy 720Li with no obvious effects of tool wear or material spring-back.

A notable characteristic that all the images collected highlighted that a band of heavy deformation exists close to the scratch surface whilst a larger and less deformed band exists surrounding this. These will be termed the heavy deformation and deformation bands respectively.

Table 6. Confocal Microscopy Confirmation of Replica Scratch Depths.

Scratch Technique	Target Depth (µm)	Actual Depth (µm)	Tip Radius[1] Average (µm)	Scratch Angle[2] Average (°)
Single-pass	25.4	25.11	52.46	90.53
	50.8	47.21	51.06	94.47
	76.2	73.42	49.79	92.97
	101.6	102.09	49.91	91.93
	127	120.72	51.06	91.66
	177.8	170.80	52.14	92.09
	254	250.75	53.00	92.16
Single-pass	25.4	27.19	50.37	92.18
	50.8	46.03	42.15	94.77
	76.2	73.20	48.44	94.66
	101.6	98.15	49.80	92.59
	127	121.43	42.17	91.71
	177.8	171.92	51.40	92.99
	254	246.40	57.83	91.56
Single-pass	25.4	29.89	46.94	89.65
	50.8	47.26	47.39	95.36
	76.2	75.12	39.41	95.21
	101.6	96.93	45.67	92.32
	127	118.85	42.01	94.26
	177.8	168.28	47.63	93.24
	254	242.11	53.85	92.67
Multi-pass	177.8	166.76	48.85	92.05
	127	121.29	49.55	91.47
	76.2	73.54	47.72	94.92

[1] Target Tip Radius – 50 µm.
[2] Target Scratch Angle – 90°.

8.4 Degree of Deformation

SEM and optical microscopes were used to examine the microstructural changes caused by the deformation process. The differences

and trends were analysed in response to scratch depth, scratch creation technique and tool position, i.e. exit and entry deformation.

8.4.1 Deformation Depth at Scratch Mid-Length Location

Scratches at each depth were cut in the transverse direction at a central point to estimate any influence of tool entry or tool exit at this stage. Specimens were then mounted in Bakelite before polishing to 1 μm finish. ImageJ software was used to measure the visible grain deformation at each scratch depth. Figure 8-2 highlights the magnified microstructural deformation associated with a scratch depth of 76.2 μm in contrast to 254 μm in Figure 8-1. There are visible regions of deformation and heavy deformation close to the scratch surface. It can only be assumed at this point that a higher hardness and hence better mechanical properties in terms of fatigue life can be found in the heavily deformed region.

There is a strong trend between depth of scratch and the visible deformation zones size. Deeper scratches increase the degree of heavy deformation in the root area as the material undergoes a cold working process which causes compressive deformation of the grains locally. The relationship between scratch depth, which relates to the applied force causing work-done to the material, and visual depth of heavy deformation is not linear as show in Figure 8-3. At the shallower scratch depths very little work is done to the material which is reflected by the low degree of heavy deformation under high magnification SEM imaging. At the increasing scratch depths the deformation zone growth rate initially increases and then reduces.

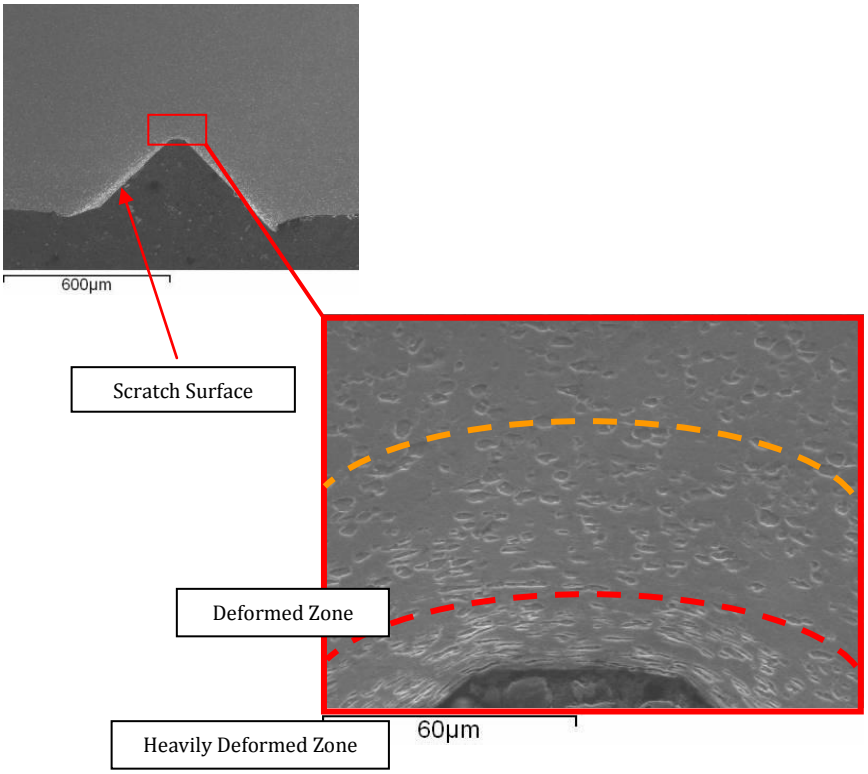

Figure 8-1. Deformation Zones at 254 µm Single-pass Scratch Depth

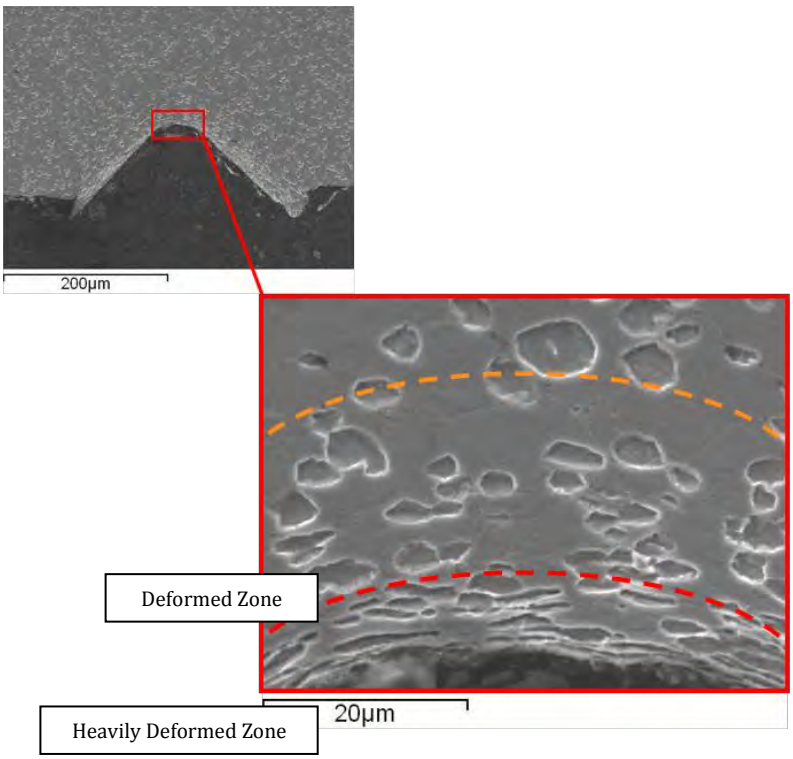

Figure 8-2. Deformation Zones at 76.2 µm Single-pass Scratch Depth

However, as the scratch depths increase the degree of heavy grain structure deformation around the scratch tip also appears to increase in magnitude. This shows that the visual methods alone are not a fully representative measure of material condition at each depth. The higher density of local precipitation strengtheners, seen in Figure 8-2 and Figure 8-1 indicate that a higher hardness exists locally which visual techniques cannot fully characterise.

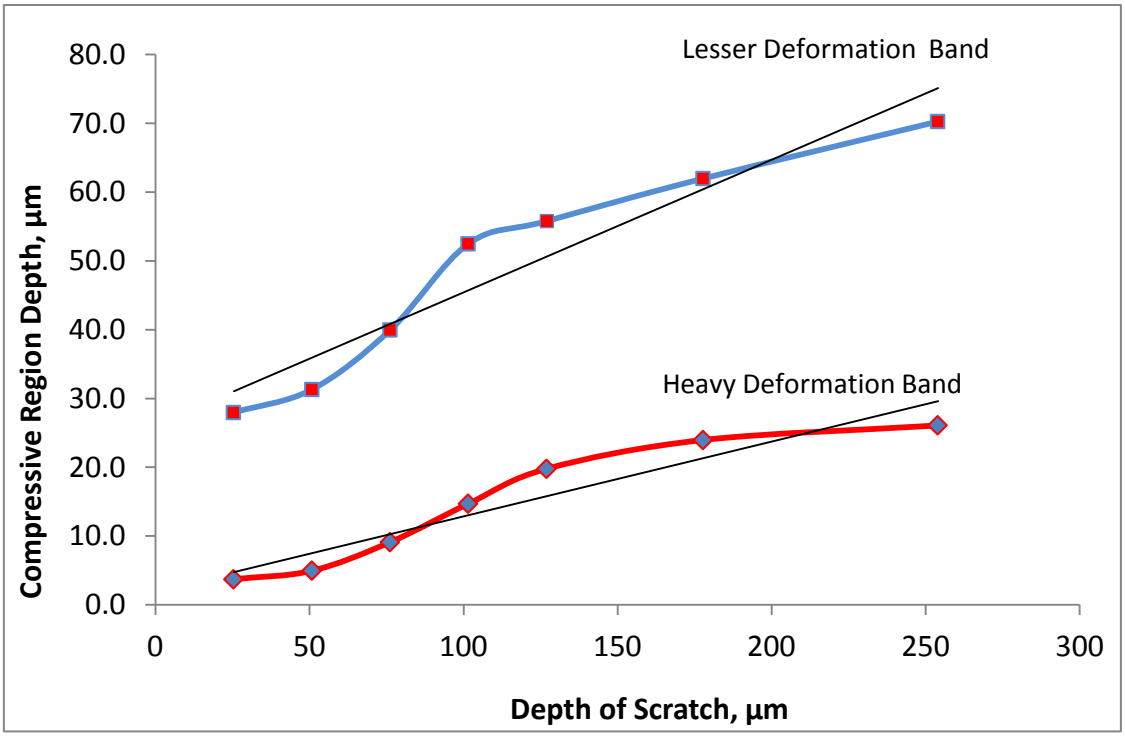

Figure 8-3. SEM and Optical ImageJ depths of deformation banding at each scratch depth.

The relationship between deformation zone and scratch depth shown in Figure 8-3. The non-linearity and reduction in deformation depth growth rates at greater scratch depths suggests that the damage mechanism changes. At greater scratch depths deformation may reached a saturation point and

cutting becomes the easier mechanism. Cutting would compressively deform the grain structure less and simply remove a greater amount of deformed material. The lesser deformation band trend data in Figure 8-3 represents the material deformed furthest from the scratch surface. The trend follows that of the heavy deformation band data indicating that the degree of deformation is governed by the heavily deformed zone profile.

8.4.2 SEM Characterisation of Tool Entry vs. Exit Deformation Trends

When considering microstructural deformation along the scratch path from tool entry point to tool exit the heavy deformation zone size differs which may result in different mechanical properties. The heavy deformation zone profile does is not always symmetrical, as shown in Figure 8-4 which is a cross-section of the middle of the scratch. This profile also changes along the scratch length, which will be discussed.

Figure 8-7 and Figure 8-6 indicate that the largest deformation zone depth at the tool entry point is located towards the edge of the root tip. However, towards the tool exit point the maximum deformation depth is located towards the specimen surface at the burr locations.

This is due to the large displacements of material from the scratch path which is expelled towards the surface and is characterised by burrs shown in Figure 8-4.

When comparing the two tool positions directly the deformation zone is largest at the tool exit point. This may affect the total life by improving the

initiation life preferentially at the tool exit point. The general trends can be seen in Figure 8-5, Figure 8-6 and Figure 8-7.

Most notable is the fact that the largest deformation zone does not occur at the scratch root tip. The extent or degree of heavy deformation appears highest at the root but this cannot be quantified visually to confirm where the peak beneficial mechanical properties may therefore exist. Alternative techniques such as EBSD and TEM techniques could be applied in the future to confirm the degree of deformation.

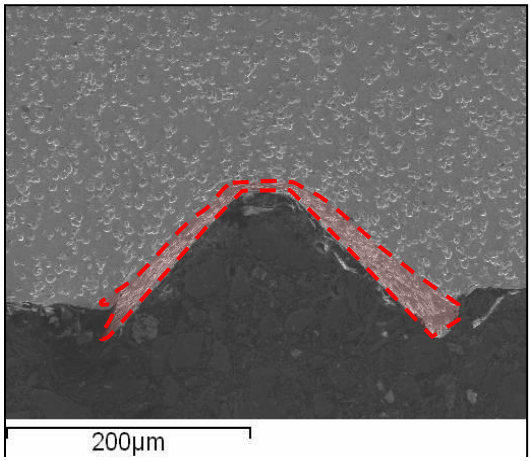

Figure 8-4. SEM image of asymmetrical heavy deformation band of 127µm single-pass scratch

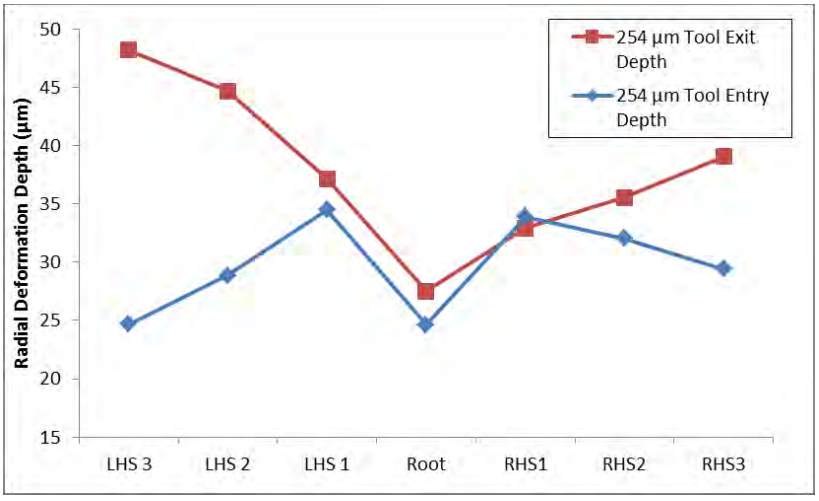

Figure 8-5. Tool exit versus tool entry deformation depth comparison at points highlighted in Figure 8-6 and Figure 8-7.

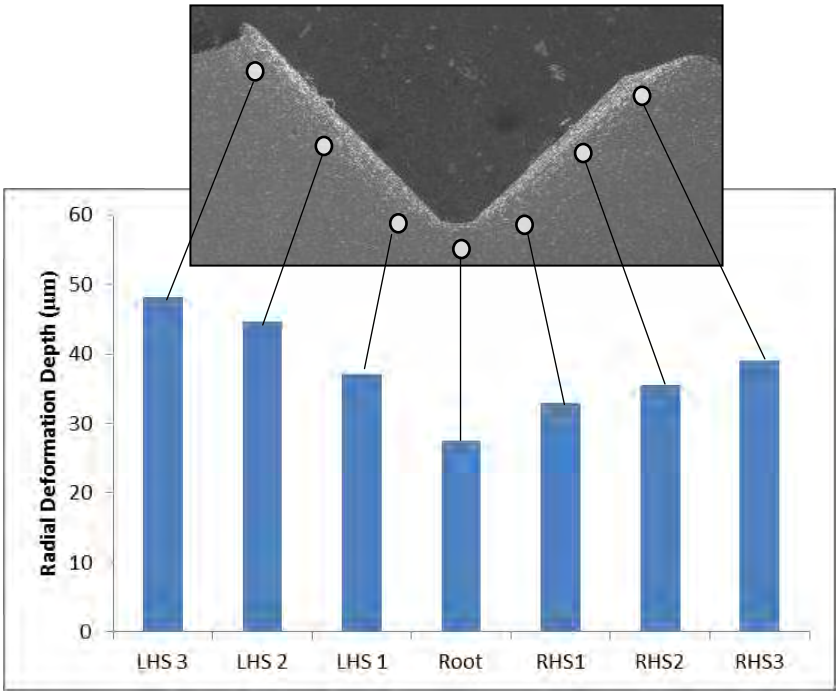

Figure 8-6. Tool exit SEM image and ImageJ measurements of heavy deformation depths for single-pass 254 µm scratch depth.

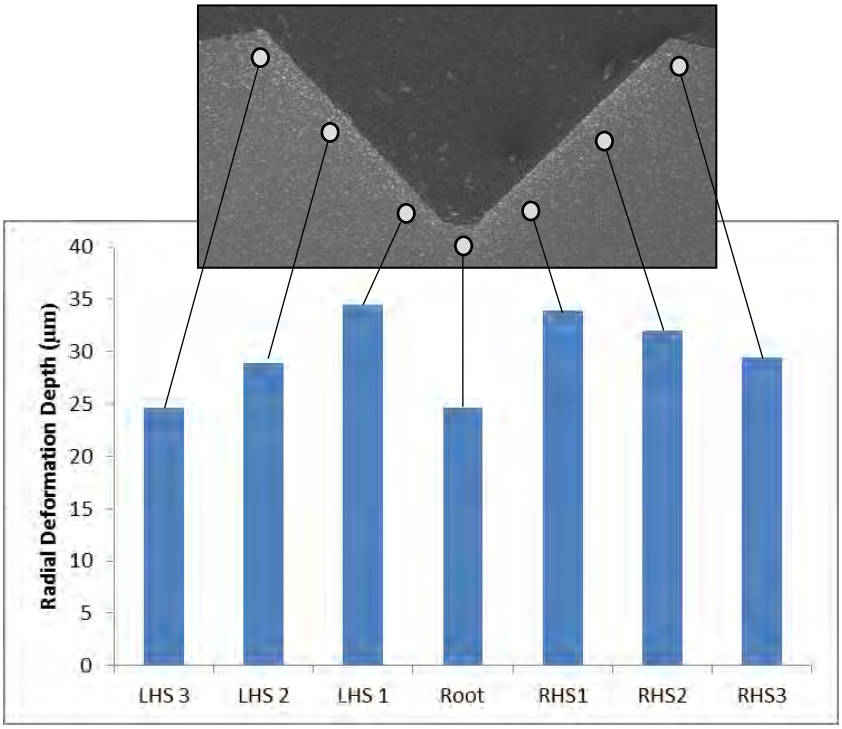

Figure 8-7. Tool entry SEM image and ImageJ measurements of heavy deformation depths for single-pass 254 µm scratch depth.

8.4.3 Micro-hardness Characterisation of Tool Entry vs. Exit Deformation Trends

The microhardness deformation maps in Figure 8-8 and Figure 8-9 show that the surrounding material is affected more around tool exit position. The tools exit point hardness average is far higher and deeper locally around the scratch. This suggests that the accumulation and densification of material as the tool moves over the surface results in a much higher hardness. This needs to be taken into account when considering other hardness maps which were taken from the centre of the scratch. These results, at 127 μm, indicating that a greater depth of deformation exists towards the surface of the specimens cross-sections, it is common across a range of scratch depths indicated in Figure 8-6 at a depth of 254 μm.

The balance between hardness and residuals stresses, both tensile and compressive, also needs further understanding as the difference in hardness doesn't seem to affect initiation locations along the scratch root. However, fatigue testing showing little clear preference between tool entry or exit position during failure. Beachmarks have indicated that initiation develops towards the tools exit point initially; this cannot be verified for non-beachmarked specimens.

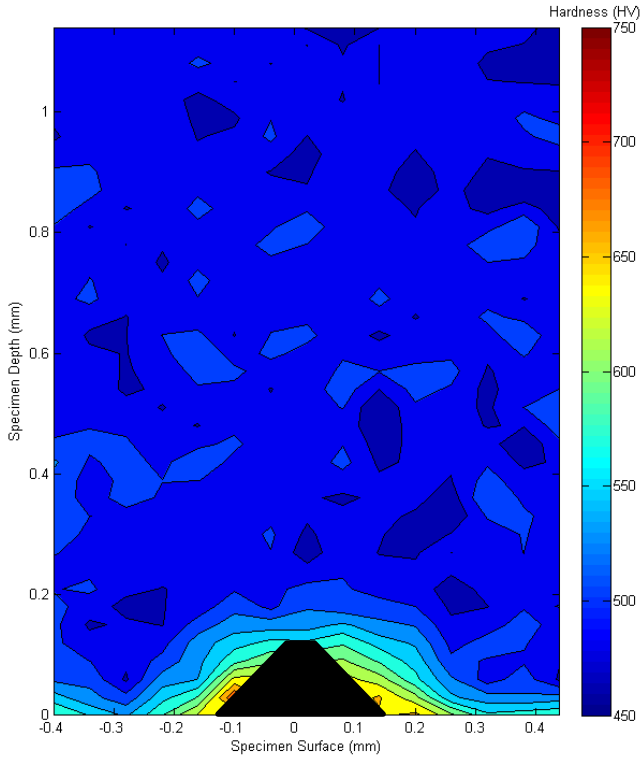

Figure 8-8. Tool entry microhardness map of multi-pass 127µm scratch depth.

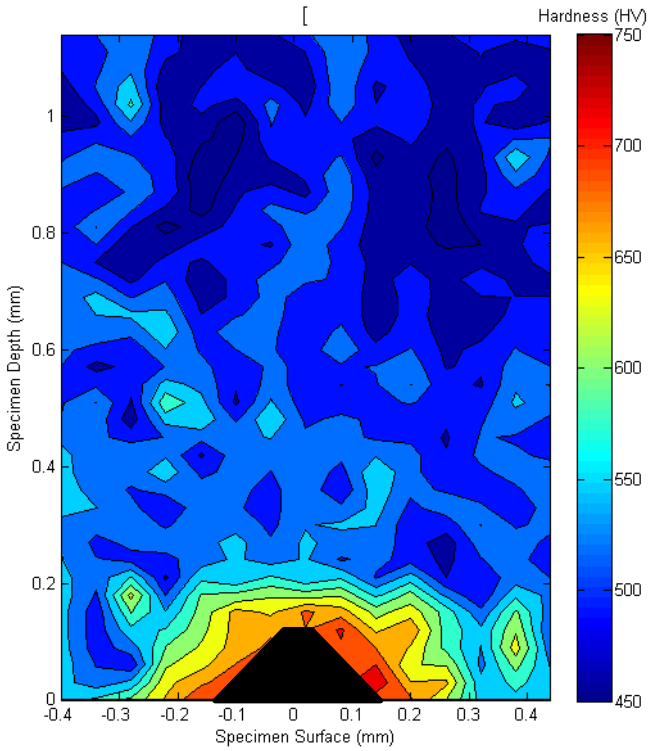

Figure 8-9. Tool exit microhardness map of multi-pass 127µm scratch depth.

8.4.4 Comparison of Single-pass vs. Multi-pass Deformation

The single pass techniques displays a significantly larger deformation zone in comparison to the multi-pass technique, compared in Table 7, at the scratch depth of 127μm as measured at the scratch root tip.

Table 7. Heavy Deformation Zone Depth for Single-pass and Multi-pass Techniques.

Scratch Techniques (Depth 127 μm)	Deformation Depth (μm)
Single-pass	19.8
Multi-pass	12.9

The increase of heavy deformation depth is approximately 35% when using the single-pass technique. At this stage it cannot be assumed that this increase is repeated for other material properties such as hardness and induced residual stress states. As seen in Figure 8-10, the deformation zone is uniformly larger for the single-pass specimens, radiating out from the scratch surface. Together with an increased deformation zone depth an increased degree of heavy deformation is also evident along the entire scratch surface for the single-pass specimens. It is likely that the compressed grains at the scratch surface that were removed with each successive pass during the multi-pass process result in a smaller heavy deformation zone.

The same deformation zone profiles exist with regards to tool entry and exit position for both multi-pass and single-pass. However, the deformation zone is larger and deformed to a higher degree at the scratch surface for the single-pass technique.

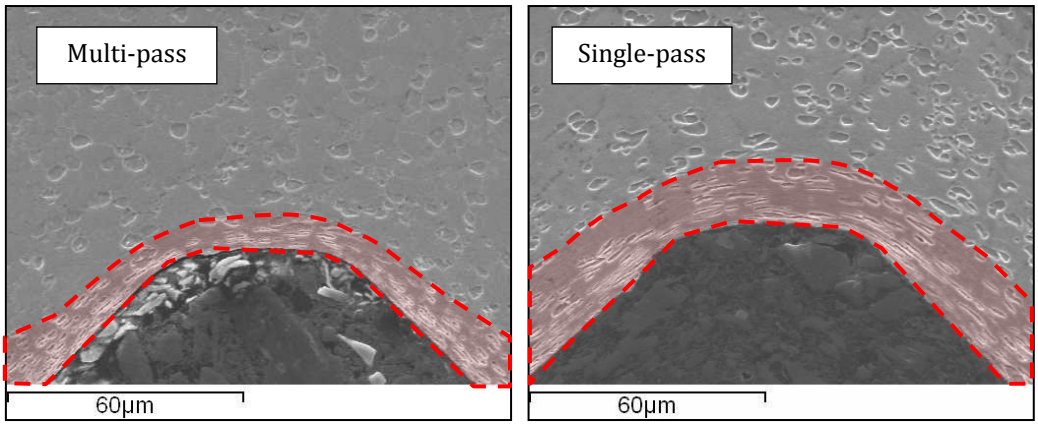

Figure 8-10. Scratch techniques heavy deformation band for 127 µm scratch depths.

8.4.5 Optical and SEM Summary

Strong trends exists which states that larger deformation zones exist at greater scratch depths. Similarly, the deformation zone and an increased degree of heavy deformation exist at increasing scratch depths. However, there appears to be a point at around 150 – 200 µm scratch depth where degree of deformation becomes the dominant feature as opposed to radial deformation zone depth.

8.5 Microhardness Evaluations

Microhardness measurements confirm that the degree of deformation and depth of elastically deformed material increase with increased scratch depths.

8.5.1 Microhardness Variation According to Scratch Depth

By plotting a series of hardness values it is possible to quantify both the degree of deformation, related to peak hardness, and the depth of

deformation zone are greater at increased scratch depths. Figure 8-11 shows that the peak hardness associated with the scratch depth of 177.8 μm is greater than 101.4 μm. When comparing lines of best fit the gradient is slightly steeper for the shallower scratch depth, however the differences in peak hardness's are similar.

In addition to simple line graph representations of hardness reduction microhardness 'map' were generated. These maps demonstrate an overview of the deformation present, shown in Figure 8-12 and Figure 8-13.

The microhardness maps confirm optical and SEM observations that the degree of heavy deformation and total deformation depth increase at greater scratch depths. At greater scratch depths the peak hardness is observed to increase due to the gross deformation of material locally. In general however, peak hardness values around the scratch tip and scratch surface differ marginally, especially at larger scratch depths.

Figure 8-12 and Figure 8-13 clearly show that the affected zone due to the scratching process extends further than what is visible based on SEM and optical observations at deeper scratch depths. In the case of the 177.8 μm the hardness increase is observed approximately 100 μm deeper than visual grain deformation. The local material hardness increase radiates from the scratch surface symmetrically and uniformly. This further implies that the visual heavy deformation zone does not fully represent the extent of the plastic deformation caused by the scratching processes. It is therefore

recommended that the microhardness profile and mapping is a better technique to evaluate the influence of the scratching process.

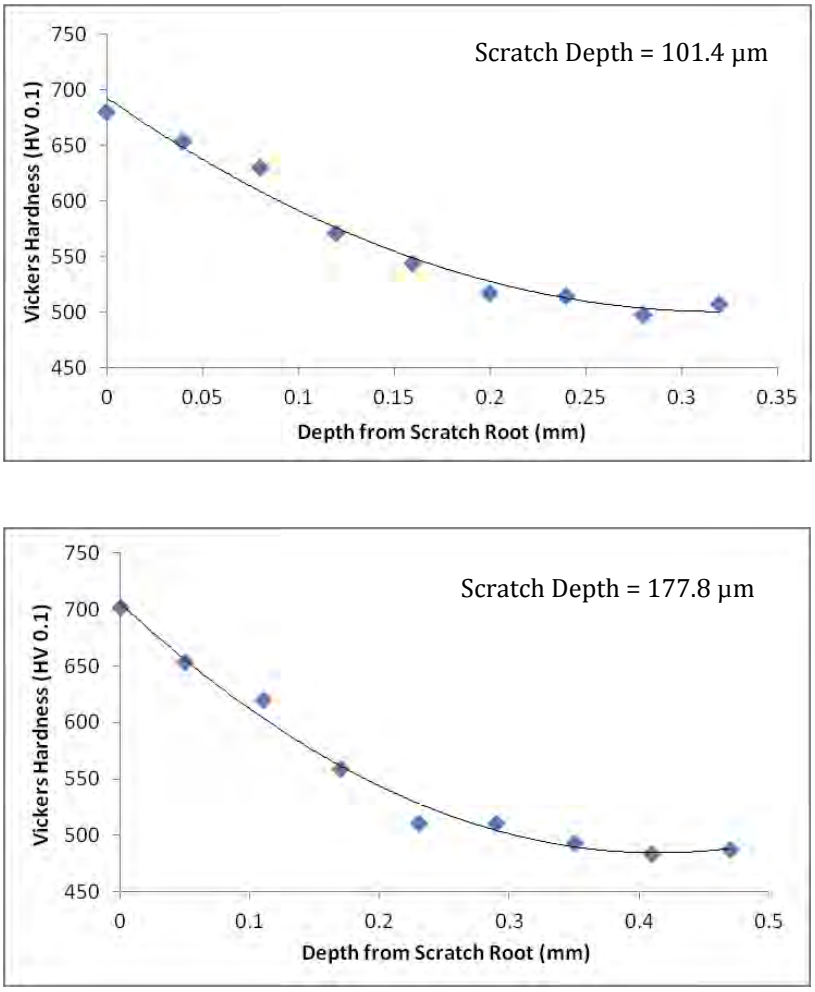

Figure 8-11. Reduction in measured hardness (HV) moving away from the scratch root tip towards bulk material at the different scratch depths indicated.

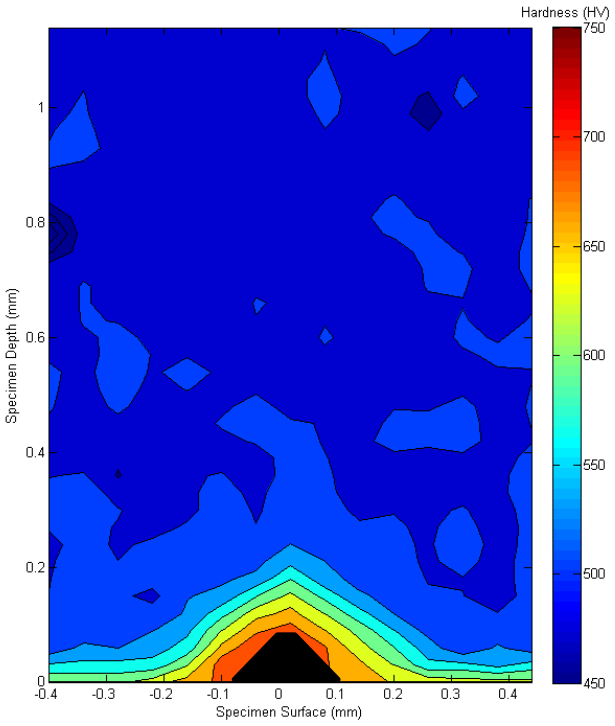

Figure 8-12. Single pass hardness map – 101.4 µm

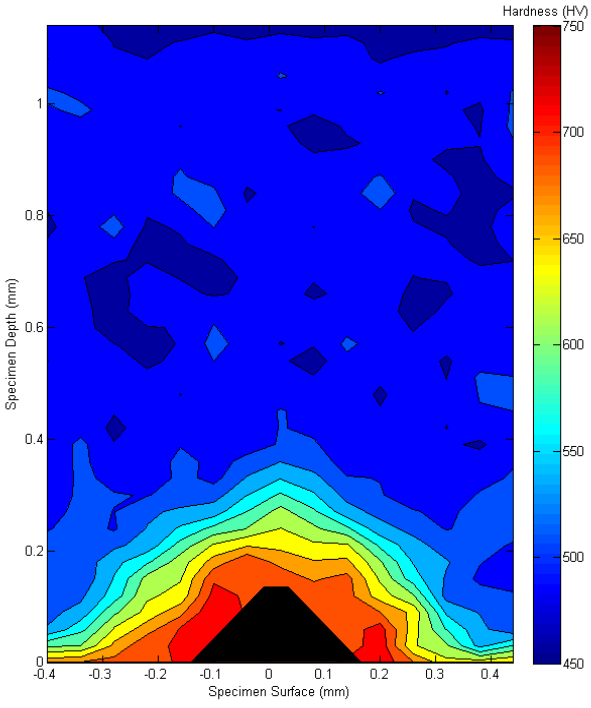

Figure 8-13. Single-pass hardness map 177.8 µm

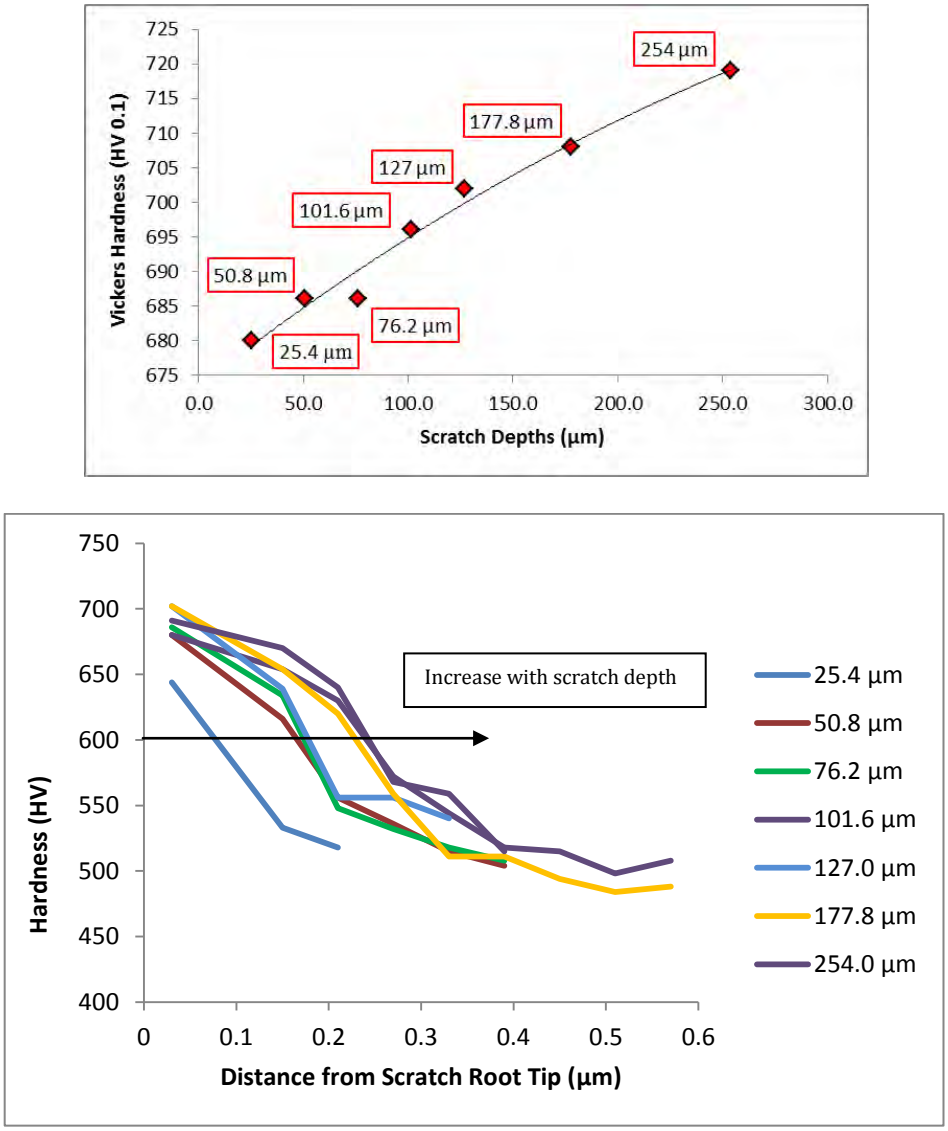

Figure 8-14. Peak hardness (top) and hardness incrementally from scratch (bottom) versus peak scratch depth.

The maximum hardness at each scratch depth has been plotted in Figure 8-14. This indicates that hardness, in general, has a more linear relationship to scratch depth and work-done than the area of visual deformation depth. Figure 8-14 also indicates that at greater scratch depths a given hardness (600 HV) exists at increased depths, respectively.

8.5.2 Microhardness Comparison of Single-pass and Multi-pass.

The effected zone depth is similar for both scratching techniques. However, the peak hardness of the single-pass technique is higher than multi-pass, this correlates with a larger degree of grain deformation in Figure 8-10. This may suggest that the depth of any compressive residual stress which may be present is similar for both techniques. However, higher peak hardness values measure in single-pass specimens may indicate different distributions of residual stress compared to multi-pass, competitively shown by colour contours in Figure 8-15 and Figure 8-16

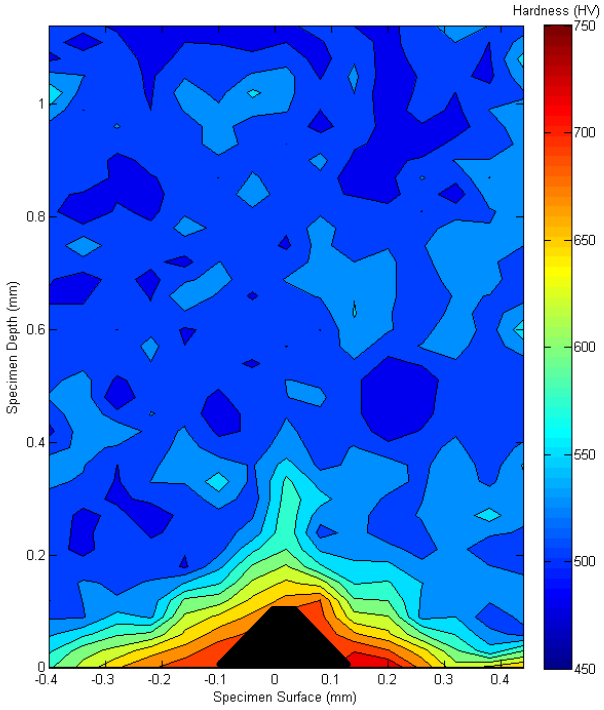

Figure 8-15. Microhardness cross-section contour plot, single-pass 127 µm

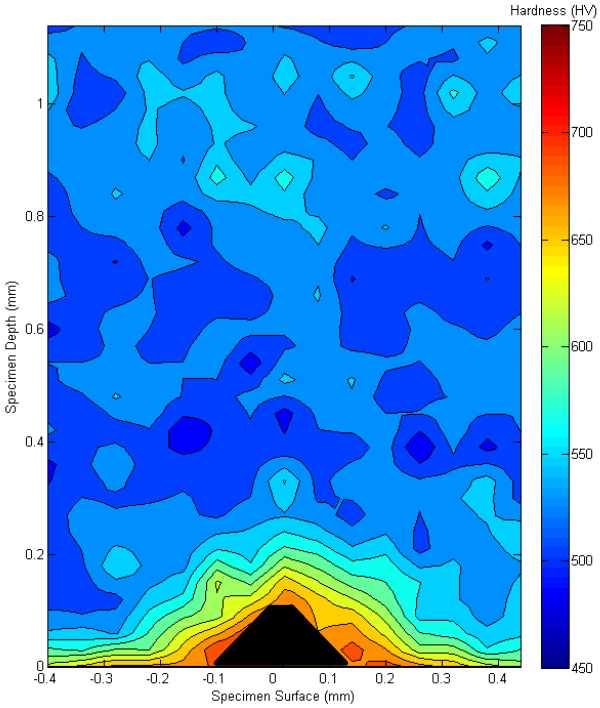

Figure 8-16. Microhardness cross-section contour plot, multi-pass 127 µm.

8.5.3 Microhardness Stress States

Huang suggested that cross-sections of hardness indentations are indications to the residual stress states in a material [47]. The theory suggests that material around an indentation will deform according to the stress states present, examples are shown in Figure 8-17.

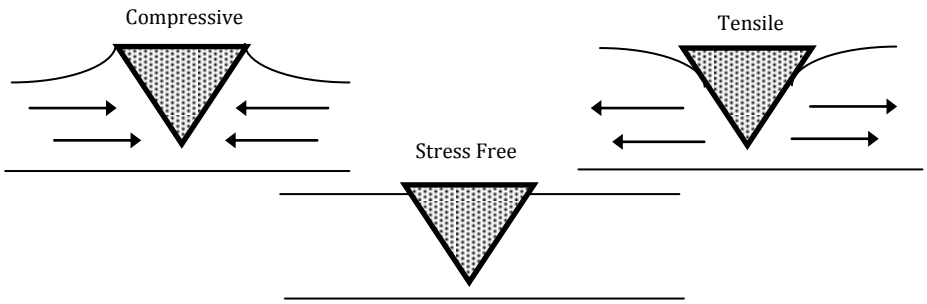

Figure 8-17. Theoretical surface undulations predicted according to apparent stress states.

A microhardness map of the shot peened layer was taken several millimetres away from the scratch on the edge of the 177.8 μm specimen shown in Figure 8-18. The depth of increased microhardness above the bulk hardness is approximately 100 μm. Therefore, localised hardness at scratch depths greater than 100 μm should not be highly influenced by the shot peened hardness layer. At surface peening conditions discussed for Alloy 720Li the compressive residual stress influences (~175 μm) are deeper than microhardness indicate (~100 μm). The peak hardness of ~670 HV coincides with surface residual stresses of 550 MPa compressive. Coincidentally, the residual stress observed at the minimum point of notable increased hardness (~100 μm) is also approximately 550 MPa as the residual stress profile reaches a peak sub-surface and diminishes approaching tensile states. However, the specimen preparation processes, i.e. cutting and polishing, will have diminished the residual stresses present further so microhardness measurements still remain complex to estimate.

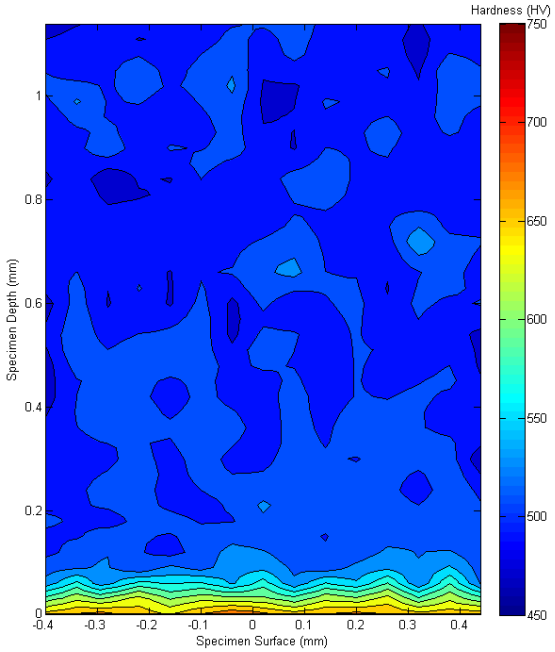

Figure 8-18. Shot Peened Layer Microhardness Map

Figure 8-12 and Figure 8-13 indicates that when a scratch is present an extensive hardness increase can be observed. As the area of increased hardness is far greater than the visual grain deformation other influences must be responsible.

The Olympus Lext OLS 3100 software allows an area surface height measurement to be taken across hardness indentations shown in Figure 8-19. This can then be averaged to give an overall indentation profiles shown in Figure 8-20 - Figure 8-22.

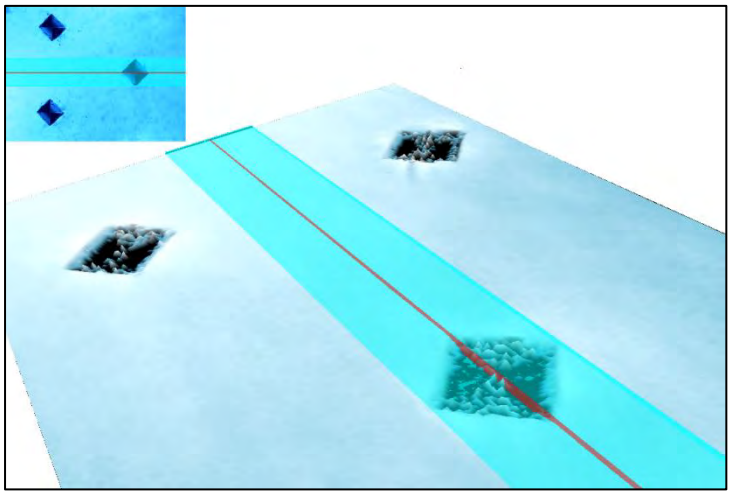

Figure 8-19. Confocal z-axis area averaged height analysis method.

Hardness indenter profiles can be viewed without damaging the specimen due to the non-contact methodology confocal analysis provides. The Olympus Lext OLS 3100 software produces profile displays of the indenter depth. Reassuringly, it is observed that further from the scratch surface the measurement taken results in larger indentations, i.e. softer material.

More importantly, the indenter profile shape may indicate the stress-state present at each point as suggested by Huang [47]. Figure 8-20 is closest to the scratch tip, the profile suggests that a small tensile residual stress is present, characterised by the outwardly sloped specimen surface. The next indentation, Figure 8-21, was performed 40 µm away from Figure 8-20 away from the scratch surface. The gathering of material around the indenter is a strong indication that a compressive residual stress exists. The final indentation profile is positioned 0.98 mm from the scratch tip and shows no

apparent stress-state which is expected further away from the residual stress field.

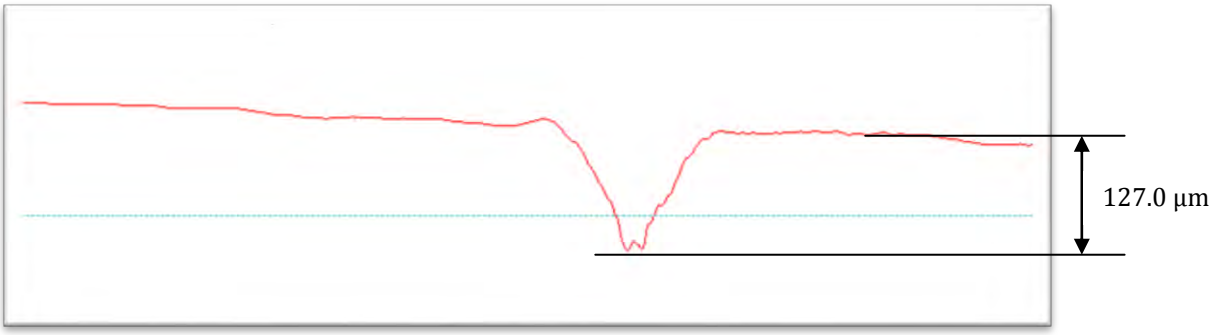

Figure 8-20. Confocal cross-section of scratch root tip indentation, 127.0 µm scratch depth (1000 x mag.)

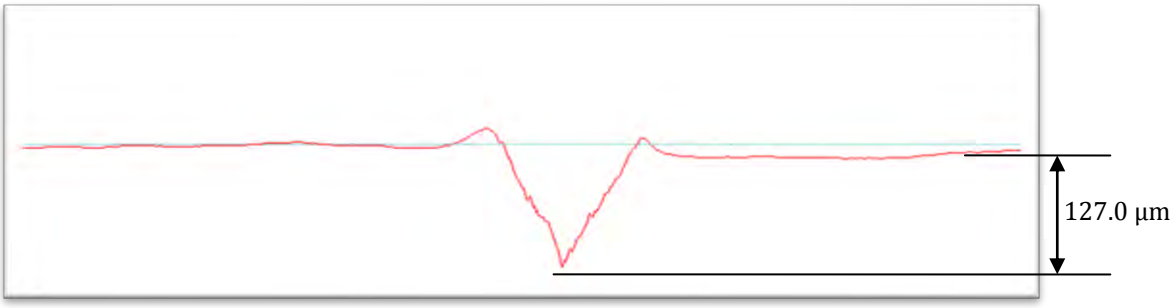

Figure 8-21. Confocal cross-section of scratch root tip + 40µm indentation, 127.0 µm scratch depth (1000 x mag.)

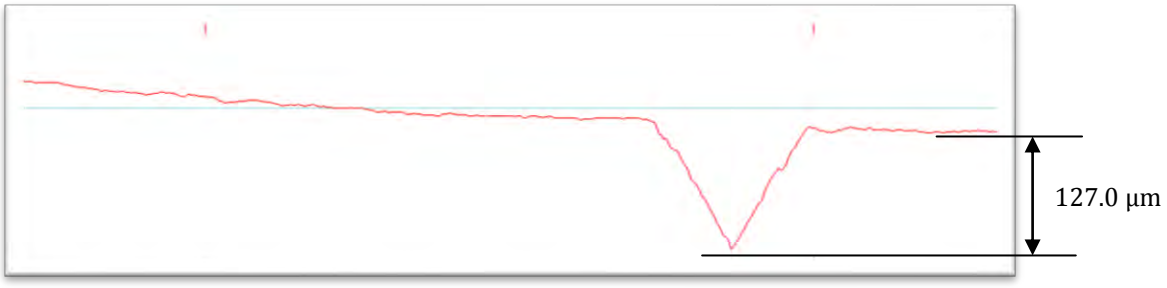

Figure 8-22. Confocal cross-section of scratch root tip + 900 µm indentation, 127.0 µm scratch depth (1000 x mag.)

An alternative method of evaluation to illustrate this effect may be to incrementally grind down the cross-section surface and repeat indentations.

8.5.4 Microhardness Summary

Pawade et al. suggested a quantification value, DWH(%), to quantify the degree of work hardening (DWH) shown in (15). This acts as a basic guideline value to compare different scratch depths and processes.

$$DWH(\%) = \frac{MH_S - MH_B}{MH_B} \times 100 \tag{15}$$

HM_S and HM_B represent the microhardness at the surface and bulk respectively. The calculated values for different scratch depths are shown in Table 8, it shows that the DWH parameter increases at greater depths.

Table 8. Degree of Work Hardening. Single-Pass - (s), Multi-Pass - (m)

Scratch Depth (µm)	127 (s)	127 (m)
DWH(%)	30.9	26.6

Scratch Depth (µm)	25.4 (s)	50.8 (s)	76.2 (s)	101.6 (s)	127.0 (s)	177.8 (s)	254 (s)
DWH(%)	28.8	29.4	29.4	30.4	31.1	31.6	32.6

The hardness maps show that the material properties have been affected far beyond what SEM inspections indicate. It also shows that competitively high hardness locations coincide with the greatest depth of heavy deformation locations at the scratch tip and towards the specimen surface and scratch burrs.

This proves that beyond the obvious grain deformation additional stress-states exist. Microhardness analysis suggests a small tensile and larger

compressive residual stress area exists at the scratch tips caused by the scratching process.

8.6 Low Cycle Fatigue

A series of high temperature, uniaxial fatigue tests were performed jointly between Rolls-Royce and the University of Birmingham. The primary focus of this analysis concentrates on the Kt 1.1 notched specimens at 600 - 650°C. Specimens with scratches at different depths produced by multi-pass, single-pass and scratch free were tested for comparison at a wide range of applied net stresses.

8.6.1 Initiation Analysis

Fatigue cracks were observed on the fracture surface to have multiple initiation sites all forming along the scratch root, see Figure 8-24. These sites are observed, shown in Figure 8-23 on a 100,000 cycle run-out specimens, connect along the length of the scratches to form long and shallow fatigue crack arc which later grew into conventional thumbnail cracks.

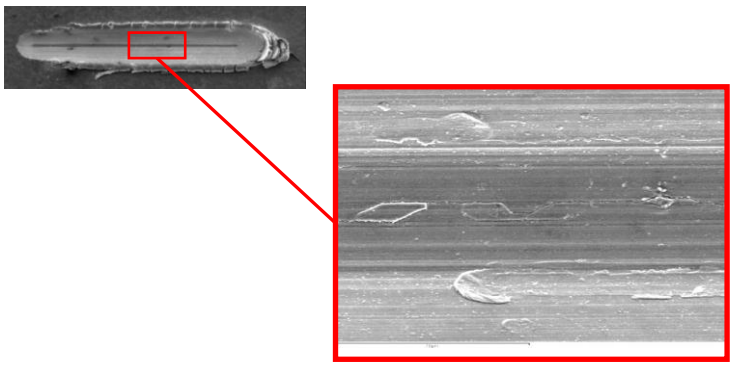

Figure 8-23. Coalesced Cracks Along Run-out Specimen Root

No subsurface initiation was observed in testing at Rolls-Royce or subsequent tests at the University of Birmingham.

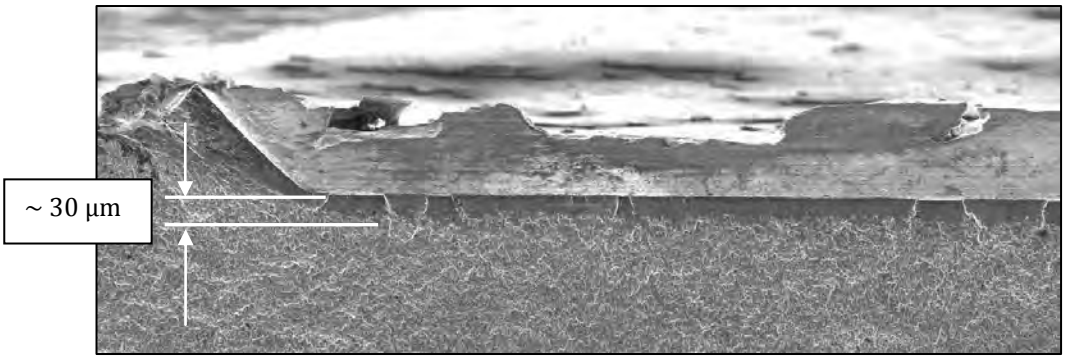

Figure 8-24. Multiple fatigue crack initiation points and transgranular region.

No preferential bias was found between tool entry or tool exit initiation. The majority of fatigue arcs were observed to initiate from the uniform base of the scratch. This is likely due to the highest stress concentration factors being found at the notch locations within the specimen geometry, shown in Figure 8-25, and in the presence of the scratch damage features. Simple linear-elastic finite element modelling using Abaqus 6.9-1 and CAE software package supports this assumption. The peak stress regions, denoted by red, are shown in Figure 8-25.

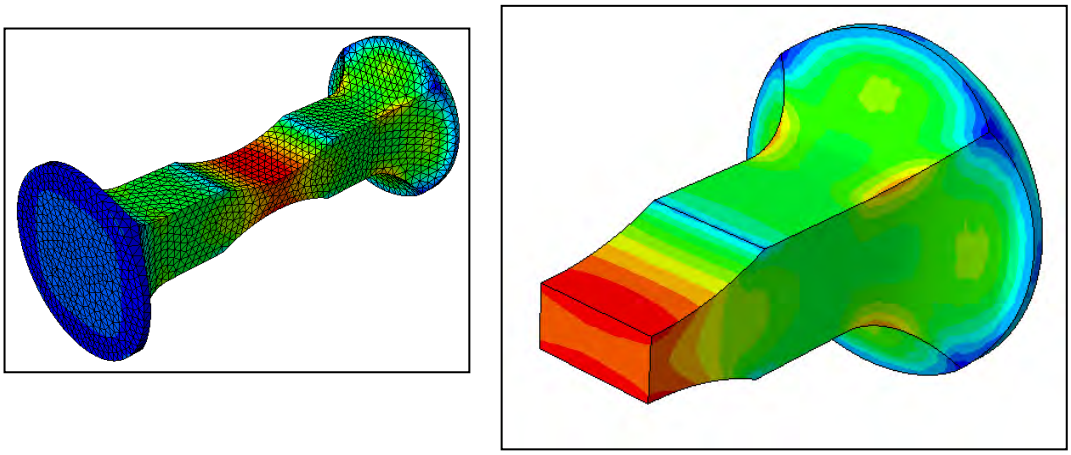

Figure 8-25. Linear elastic Abaqus FE modelling of kt notch stress profiles.

This will be accentuated in the presence of a scratch but simply serves to demonstrate that the highest stress is generally in the centre of notched specimens of this type.

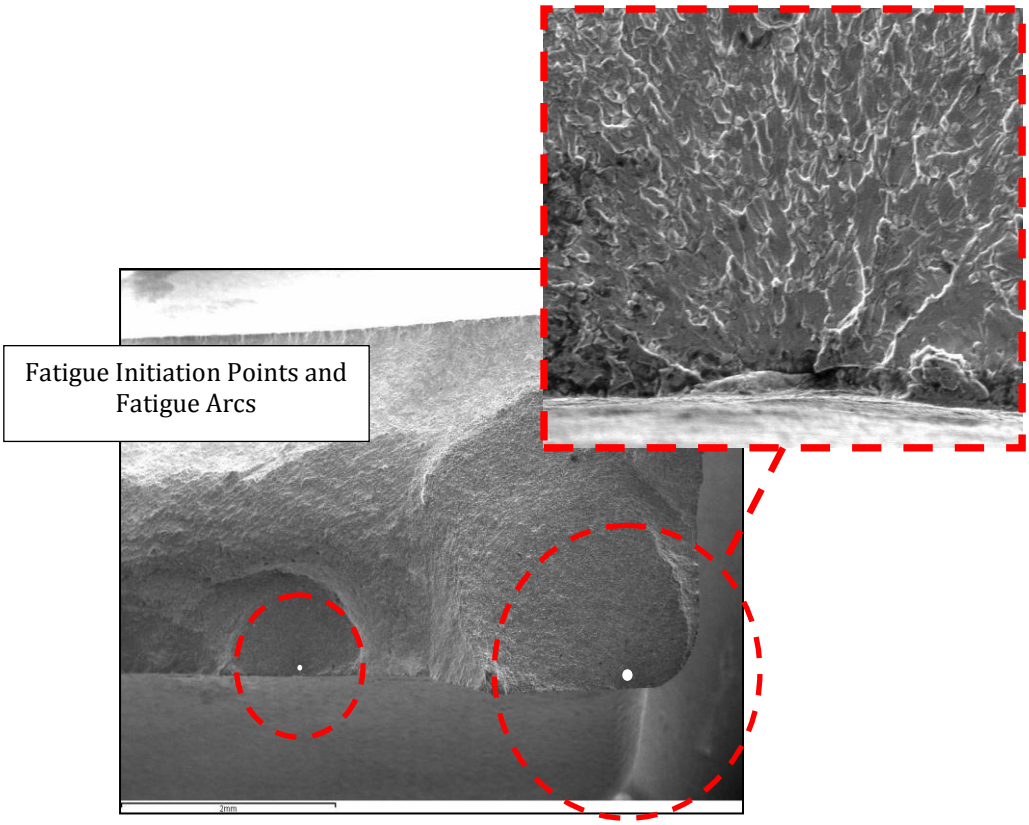

Figure 8-26. Unscratched Specimen Initiation, 1-1-1-1, 600°C, 1300 MPa

A series of fatigue tests were performed on unscratched notched specimens for baseline purposes. Several specimens failed at thermocouple and DCPD weld positions. In addition however, a wide range of scatter was found as initiation ranged from 1951 cycles to 100,000+ run-out tests. A check was performed to ensure surface roughness due to shot peening was not significantly contributing to initiation in failed unscratched specimens. Whilst initiation site originate from deeper dents, introduced by shot peening

and shown in Figure 8-26, all cracks were all found to be in the vicinity of the high stress concentration location, shown in Figure 8-27 which corresponds to the high stress region in Figure 8-25.

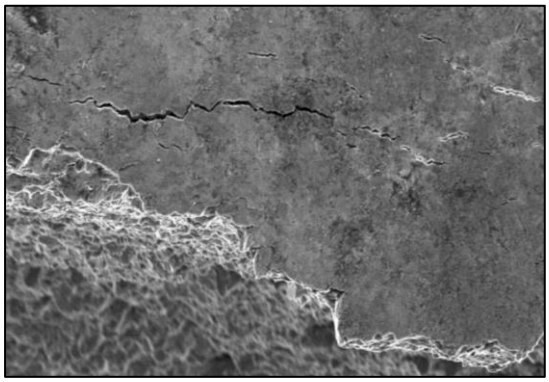

Figure 8-27. Surface Initiations Un-notch Specimen.

Surface roughness analysis proved to be within tolerance with an acceptable R_a value of 1.186. The analysis was completed on the Olympus Lext Confocal microscope shown in Figure 8-28.

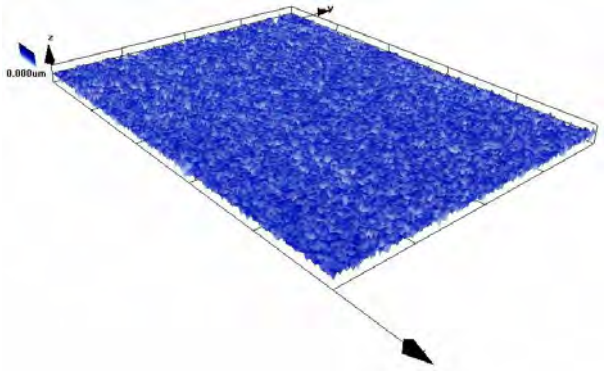

Figure 8-28. 3D Shot Peened & Untested Surface Roughness Map

In general, at both 1-1-1-1 at 600°C and 1-60-1-1 at 675°C test conditions the cycles to failure life is longer in the presence of a shallower scratch, as expected. S-N data from these Kt1.1 tests are shown in Figure 8-29 and Figure 8-30.

At the higher temperature 675°C and dwell waveform of 1-60-1-1 no strong trend is present suggesting that the influence of scratch depth at depths of 101.4 and 177.8 µm is not the primary driving factor. This is potentially caused by relaxation of the compressive residual stress at higher temperatures.

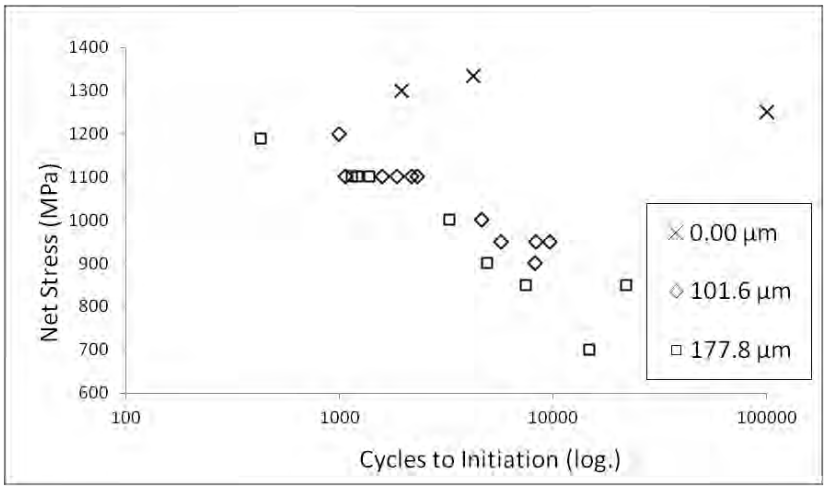

Figure 8-29. S-N Initiation Data: 1-1-1-1, 600°C

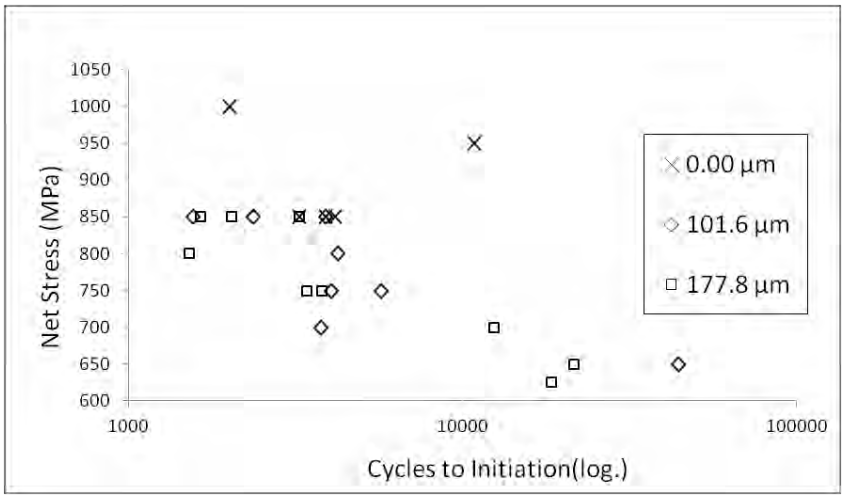

Figure 8-30. S-N Initiation Data: 1-60-1-1, 675°C

Surface oxidation can be seen in Figure 8-31 but would not influence initiation at the exposure times and temperatures used, e.g. 600°C after ~19hrs.

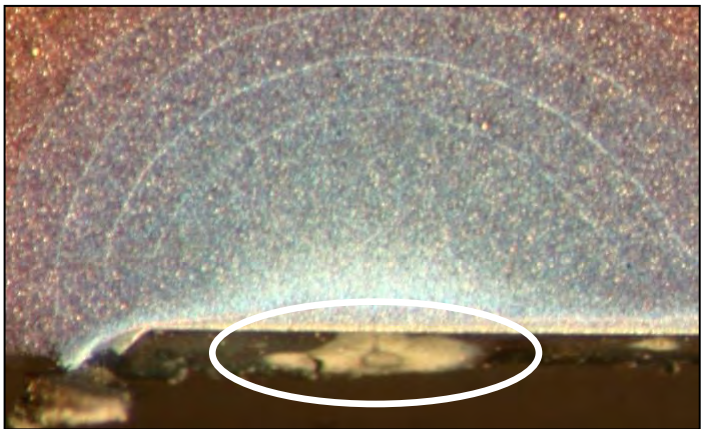

Figure 8-31. Localised oxidation at origin of thumb-nail crack on calibration specimen

8.6.2 Propagation Analysis

The proportion of total life spent at crack propagation reduces as scratch depth increases. When comparing the 600°C 1-1-1-1 tests against the 675°C 1-60-1-1 tests the proportion of total life spent during propagation is severely reduced under the combined influence of dwell and increased temperature, shown in Figure 8-32 and Figure 8-33.

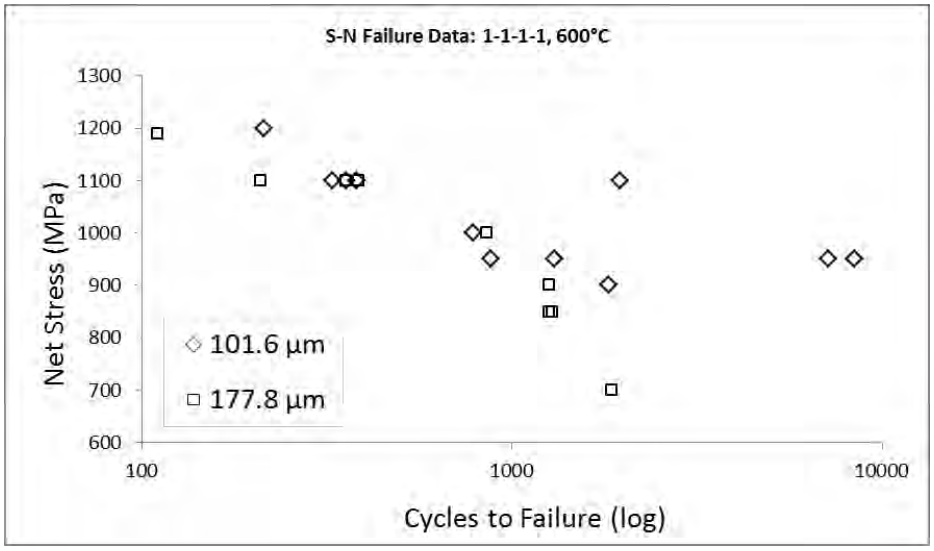

Figure 8-32. Proportion of total life spent at propagation, 1-1-1-1 600°C

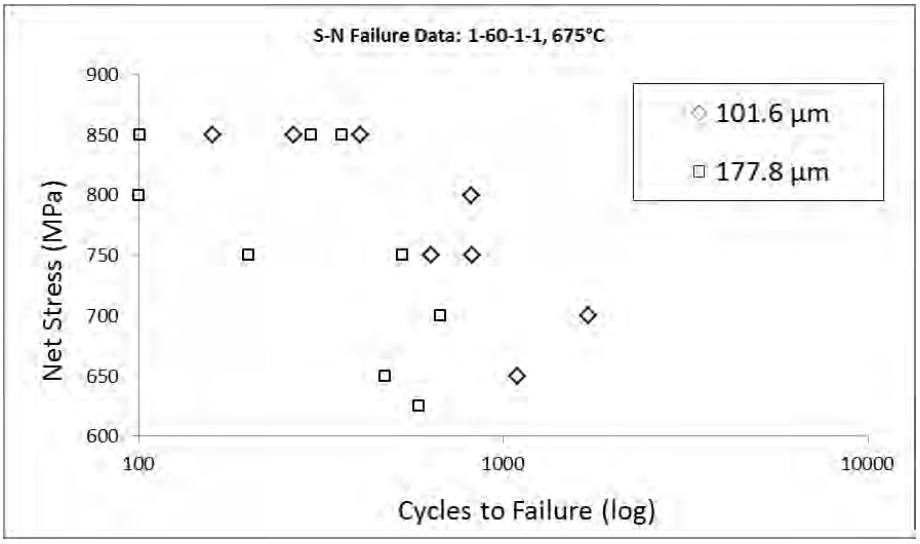

Figure 8-33 Proportion of total life spent at propagation, 1-60-1-1 675°C

During high Kt factor testing the effect of temperature alone can be analysed. The proportion of total life spent during propagation is reduced at higher temperatures due to the increased ductility. Interestingly at greater scratch depths the numbers of cycle at propagation increases, this is potentially a result of scatter or increase in depth of compressive deformation. Further detailed analysis is required, results are shown in Figure 8-34.

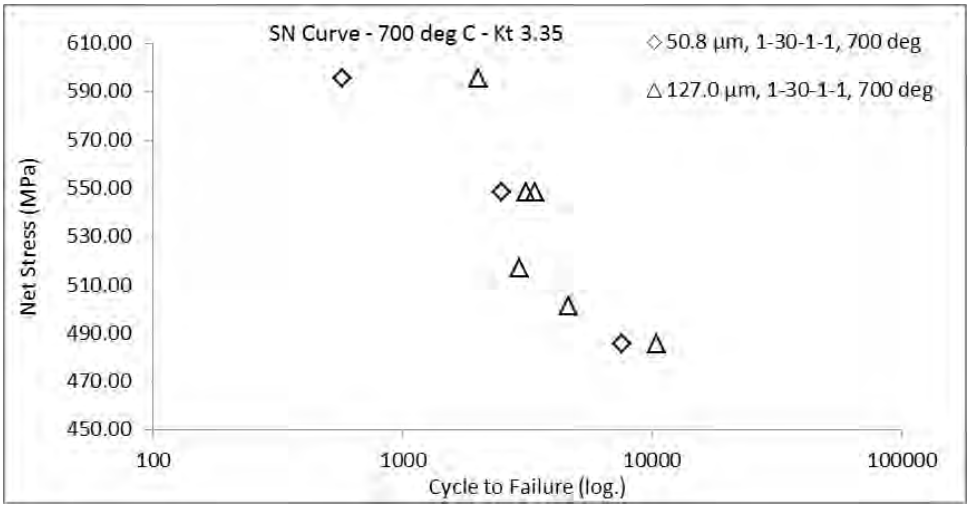

Figure 8-34. Propagation life and scratch depth comparison at Kt 3.35 700 °C.

In general, at greater scratch depths there are fewer cycles to failure across all test parameters, i.e. temperatures, scratch depths and Kt factors. This trend becomes less apparent at higher net stresses where applied load becomes the heavily dominant influence. Specimens with no scratch present exhibit very short proportion of total life spent at propagation in all cases.

Several crack growth morphologies have been observed across all test scenarios. In general cracks feature a fracture-less transgranular morphology which may suggest rapid crack growth within that region.

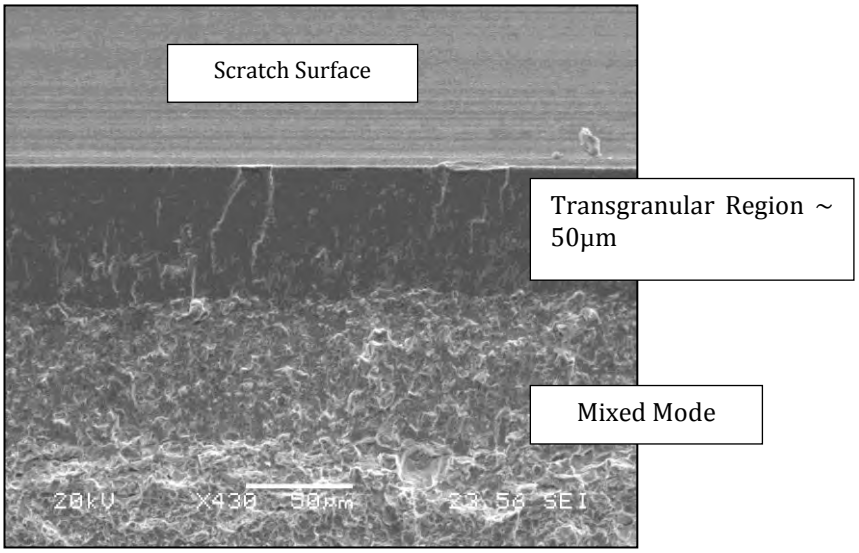

Figure 8-35. Transgranular Crack Morphology

Typical fracture surfaces are seen in Figure 8-35. Crack growth progresses to mixed mode and in some cases intergranular at high net stress, see Figure 8-36.

Cracks have been shown to exhibit shallow growth as initiation site coalesce and then develop in the conventional thumb-nail shape until

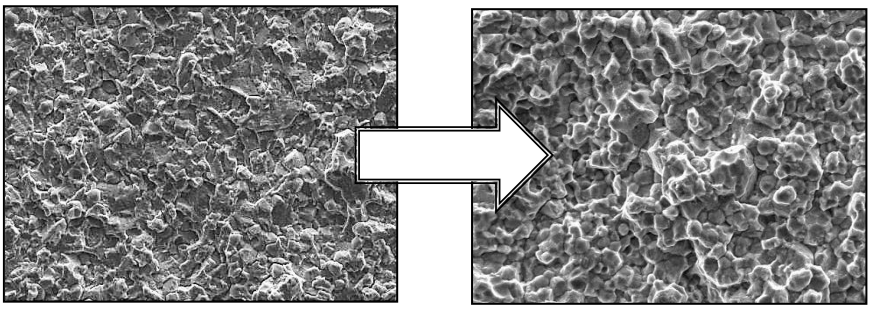

Figure 8-36. Mixed Mode (a) and Intergranular (b) Transgranular

fracture, shown in Figure 8-37. At the point where two thumb-nail fatigue arcs meet there is a region linking the two arcs where fast fracture occurs.

8.6.3 Dwell Fatigue

Additional methodical testing is required to analyse the effect of dwell crack growth in the presence of scratches. In general the propagation lives of all dwell tests are lower. The 1-60-1-1 cycle times are lower than the 1-1-1-1 cycles at Kt 1.1 but the influence of higher temperature during the

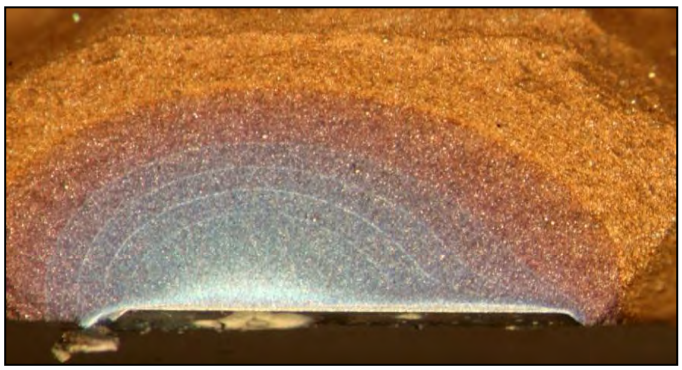

Figure 8-37. Fatigue Crack Growth Shape

dwell tests cannot be ignored. When examining the fracture morphology there is a noticeable increased in the transgranular region depth which can be seen in Figure 8-38.

Figure 8-38. Dwell Crack Growth Transgranular Region

8.6.4 Scratch Depth

For Kt 1.1 specimens both fatigue initiation and failure lives decrease as scratch depth increases, excluding individual erroneous results shown in Figure 8-29 and Figure 8-32. At 675°C, 1-60-1-1, and approaching 850MPa this trend is not conclusive. At very small scratch depths there appears to be no effect in terms of total life. This results from the beneficial influence of the compressive shot peened layer.

At higher stress concentration factor such as Kt2.0 and Kt3.35 specimens there is evidence of an inverse relationship between scratch depth and total life. Figure 8-39 and Figure 8-40 indicate that although unscratched specimens have the longest life 50.8 μm (0.002) specimens appear to have a

marginally greater fatigue crack initiation resistance compared to 127.0 µm (0.005) specimens. The apparent inverse relationship between scratch depth and fatigue life is not conclusive and requires a more structured and tailored testing approach. One potential explanation is that the increased residual stress, caused by the additional work-done creating the scratch at this depth, protects the scratch tip from initiation.

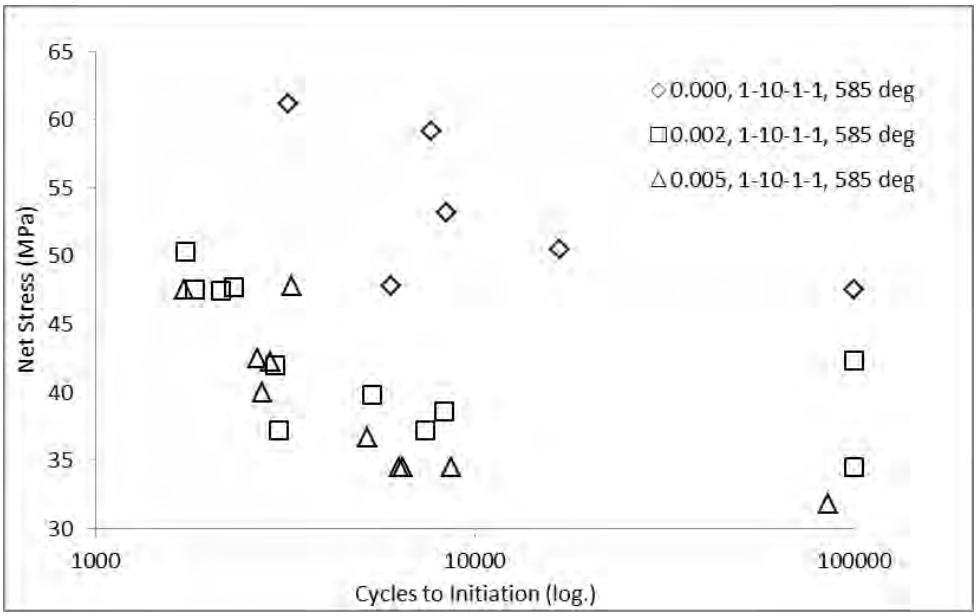

Figure 8-39. Initiation - Kt2.0, 565°C

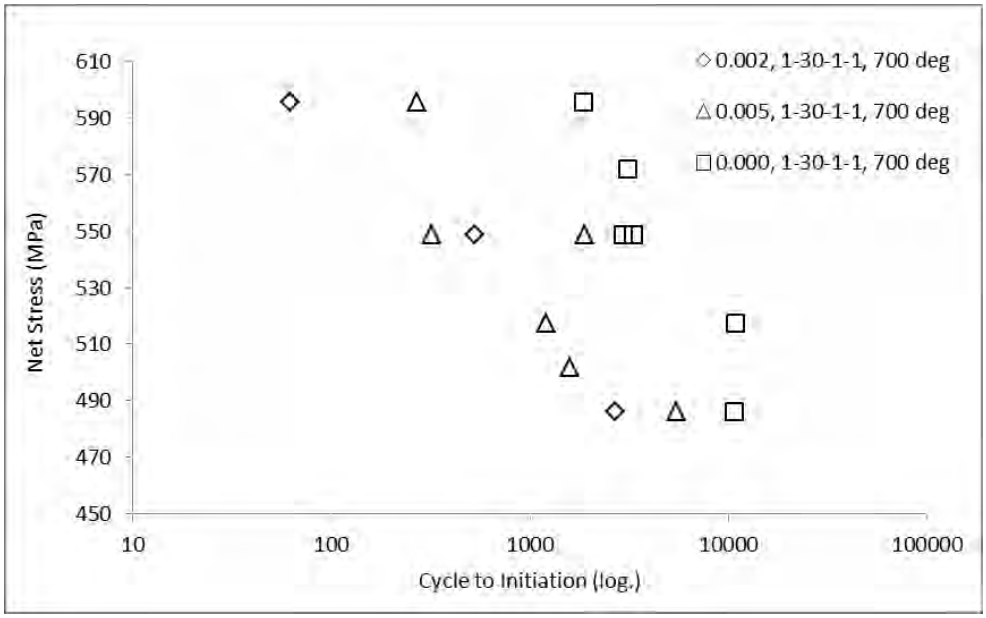

Figure 8-40. Initiation – Kt3.35, 700°C

8.6.5 Scratch Creation Technique

Preliminary tests have been conducted at 600°C to assess the total life effect of different scratch creation techniques. The tests have shown that the total life of specimens prepared using the new single-pass technique exceeds that of the traditional multi-pass method over a range of applied stresses, evident in preliminary test performed at the University of Birmingham displayed in Table 7.

Specimens were also prepared with single-pass scratches on one notch and multi-pass on the opposite side on a single specimen. This resulted in preferential initiation at the multi-pass scratch which indicates that the increase grain deformation, hardness and any other crack inhibitors such as residual stress have a beneficial effect.

The fracture mechanisms remain the same as multi-pass mechanisms already discussed.

8.6.6 Summary

In summary there seems to be strong evidence of additional stress-states. Microhardness suggests that the degree of deformation may contribute to the fatigue crack growth resistance.

Additional research is required to analyse the effects of dwell and temperature in isolation. Further additional research is also required to assess the magnitude and effected areas of residual stress induced by both scratching processes.

8.7 Failure Mode Analysis

When analysing failure mechanisms the depth of transgranular crack growth in multi-pass specimens approximately equals that of the deformed zone. Figure 8-3 corresponds to the measured depth in Figure 8-42 of ~ 50 µm. This indicates that transgranular crack growth in multi-pass specimens shows a close relationship to visible deformation depth. Past this point mixed mode cracking is observed. Conversely, for single-pass specimens, Figure 8-41, the transgranular band is less pronounced and the depth before mixed mode propagation is more closely related to the band of heavy deformation also shown in Figure 8-3. Tensile residual stresses at the surface of the scratches could increase the driving force and hence promote rapid growth from transgranular to mixed mode growth. The increased accumulation of heavily deformed grains seen after single-pass scratch creation could reduce the effective driving force and slow the propagation rates encouraging mixed mode failure earlier.

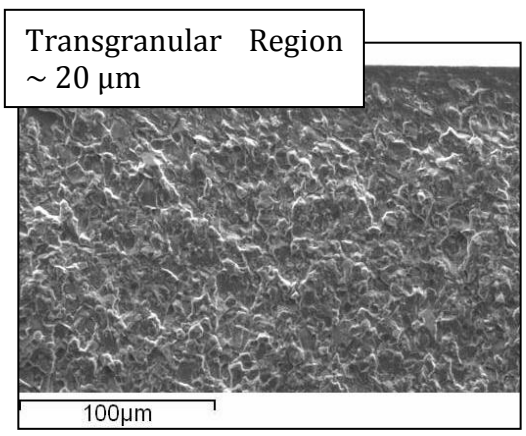

Figure 8-41. Transgranular Crack Depth – 101 µm

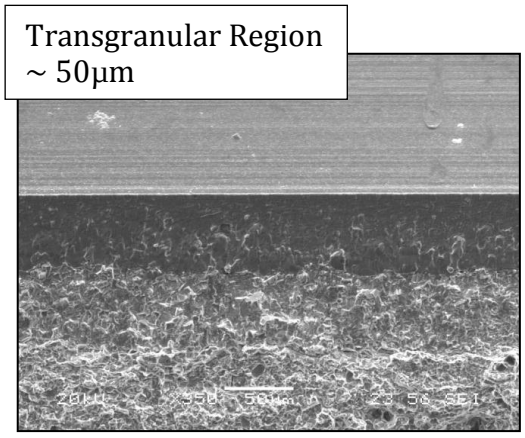

Figure 8-42. Transgranular Crack Depth – 127 µm

Chapter 9:

Conclusions and Further Work

9.1 Conclusions

Alloy 720Li has been studied in terms of its damage tolerance properties under different scratch damage conditions and test parameters.

Visual inspections of scratches at various depths were examined using optical and SEM techniques. All scratches examined were characterised by compressive grain deformation localised beneath the scratch surface. The relationship between deformation zone size and increased scratch depth is not linear as the deformed zone depth appears to reach an upper limit. The degree of grain deformation increases with scratch depth beyond the limit of optical deformation zone depth. Optical and SEM techniques highlight the difference between tool entry to tool exit deformation profiles. This suggests

that additional material is progressive deformed along the scratch length yielding a larger deformation zone and higher grain deformation densities.

However, microhardness has indicated that the visual grain deformation profile cannot be used as a full representation of the material condition. Peak hardness measurement locations successfully correlate with the peak heavy deformation zones. The microhardness maps have shown that the affected zone spans significantly further than grain deformation indicates especially at greater scratch depths. This suggests the depth of strain accumulation is deeper than the apparent zone of swept grains. The swept grain zone ceases to increase linearly with scratch depth however the degree of heavy deformation at the scratch tip root continues to increase based on swept grain zone appearance. This is supported by local hardness measurements which confirm that the hardness continues to increase. This beneficial property acts to prevent short crack initiation, preliminary results show that this is supported by fatigue testing. Finally, confocal microscopy of the indentation profiles indicated that a small tensile residual stress may exist at the scratch root surface. This may be offset by a compressive region which diminishes to a free stress state away from the scratch.

Fatigue results overall are incomplete and require further testing to make definite conclusions. In general, greater scratch depths have a detrimental effect on total fatigue life. However, initial results indicate that complex relationship exists between the beneficial residual stress created by the scratching process and the scratch depth stress concentration factor.

Signs of an inverse relationship between scratch depth and failure lives exist in some high Kt factor tests with scratches of 50.8 and 127.0 μm in depth, this relationship is not present at deeper 1778 μm depth tests. The single-pass scratch creation technique appears to increase fatigue initiation lives, compared to multi-pass at a given depth. This can be attributed to greater grain densification locally, according to optical and SEM imaging, and increased hardness peak values observed during microhardness mapping.

9.2 Further Work

Additional fatigue testing is required with the aim to quantify the effects of dwell loading waveforms. Further evaluation using fatigue testing together with simulations, using finite element analysis, and experimental diffraction or hole-drilling techniques are required to establish a stronger relationship between scratch depth, within the range of 76.2 – 1778.8 μm, and residual stress interactions from both the shot-peening process and deformation processes.

The extent of the deformation zone needs further analysis beyond the techniques used here. EBSD and TEM analyses would produce more microstructural information which would help failure mode evaluations and predictions.

References

1. Rolls-Royce, *The Jet Engine*. 1996: Rolls-Royce Plc.

2. Salomon, K.A., *Selection and development of alloys for turbine disc applications* in *Department of Metallurgy and Materials*. 2006, University of Birmingham: Birmingham. p. 71.

3. Claudio, R.A., et al., *Fatigue life prediction and failure analysis of a gas turbine disc using the finite-element method.* Fatigue & Fracture of Engineering Materials & Structures, 2004. **27**(9): p. 849-860.

4. Gabb, T.P., et al., *Fatigue resistance of the grain size transition zone in a dual microstructure superalloy disk.* International Journal of Fatigue, 2010. **33**(3): p. 414-426.

5. Reed, R.C., *The superalloys : fundamentals and applications* 2006: Cambridge University Press.

6. Dong, Y.-w., et al., *Determination of wax pattern die profile for investment casting of turbine blades.* Transactions of Nonferrous Metals Society of China, 2011. **21**(2): p. 378-387.

7. Hou, N.X., et al., *The influence of crystal orientations on fatigue life of single crystal cooled turbine blade.* Materials Science and Engineering: A, 2008. **492**(1-2): p. 413-418.

8. Smallman, R.E. and A.H.W. Ngan, *Chapter 8 - Advanced alloys*, in *Physical Metallurgy and Advanced Materials Engineering (Seventh Edition)*. 2007, Butterworth-Heinemann: Oxford. p. 447-480.

9. Gessinger, G.H., *Powder Metallurgy of Superalloys*. 1984: Butterworth-Heinemann Ltd 348.

10. Donachie, M.J. and S.J. Donachie, *Superalloys : a technical guide* 2nd ed. 2002: ASM International.

11. Smallman, R.E. and R.J. Bishop, *Modern Physical Metallurgy and Materials Engineering - Science, Process, Applications (6th Edition)*. 1999, Elsevier.

12. Sugui, T., et al., *Aspects of primary creep of a single crystal nickel-base superalloy.* Materials Science and Engineering: A, 1999. **262**(1-2): p. 271-278.

13. Hantcherli, M., et al., *Evolution of interfacial dislocation network during anisothermal high-temperature creep of a nickel-based superalloy.* Scripta Materialia, 2011(0).

14. Roebuck, B., D. Cox, and R. Reed, *The temperature dependence of Î³â€² volume fraction in a Ni-based single crystal superalloy from resistivity measurements.* Scripta Materialia, 2001. **44**(6): p. 917-921.

15. Jackson, M.P. and R.C. Reed, *Heat treatment of UDIMET 720Li: the effect of microstructure on properties.* Materials Science and Engineering A, 1999. **259**(1): p. 85-97.

16. Zhao, S., et al., *Gamma prime coarsening and age-hardening behaviors in a new nickel base superalloy.* Materials Letters, 2004. **58**(11): p. 1784-1787.

17. Devaux, A., et al., *Gamma double prime precipitation kinetic in Alloy 718.* Materials Science and Engineering: A, 2008. **486**(1-2): p. 117-122.

18. Rao, G.A., M. Srinivas, and D.S. Sarma, *Influence of modified processing on structure and properties of hot isostatically pressed superalloy Inconel 718.* Materials Science and Engineering: A, 2006. **418**(1-2): p. 282-291.

19. Yang, J.X., et al., *Topologically close-packed phase precipitation in a nickel-base superalloy during thermal exposure.* Materials Science and Engineering: A, 2007. **465**(1-2): p. 100-108.

20. Campbell, F.C., *Elements of metallurgy and engineering alloys*. 2008: ASM International 350.

21. Pook, L.P., *Metal fatigue : what it is, why it matters* Solid mechanics and its applications Vol. 145. 2007.

22. Pearce, J. *Metallic Corrosion - Stress Corrosion Cracking*. 2001 [cited 16/12/2010]; Available from: http://www.azom.com/details.asp?ArticleID=102.

23. Pang, H.T. and P.A.S. Reed, *Fatigue crack initiation and short crack growth in nickel-base turbine disc alloysâ€"the effects of microstructure and operating parameters.* International Journal of Fatigue, 2003. **25**(9-11): p. 1089-1099.

24. Sims, C.T., *Superalloys II*, ed. C.T. Sims, N.S. Stoloff, and W.C. Hagel. 1987, New York: Wiley.

25. Koul, A.K., N.C. Bellinger, and G. Gould, *Damage-tolerance-based life prediction of aeroengine compressor discs: II. A probabilistic fracture mechanics approach.* International Journal of Fatigue, 1990. **12**(5): p. 388-396.

26. Shepherd, D.P. and S.J. Williams, *New lifing methodology for engine fracture citical parts*, in *Aging mechanisms and control: Part B - Monitoring and management of gas turbine fleets for extended life and reduced cost*. 2001, RTO-MP-079(I): Manchester, UK.

27. Bagaviev, A. and A. Ulbrich, *Life assessment of turbine components based on deterministic and probabilistic procedures.* International Journal of Pressure Vessels and Piping, 2004. **81**(10-11): p. 855-859.

28. Claudio, R.A., et al., *Failure analysis of scratch damaged shot peened simulated components at high temperature.* Engineering Failure Analysis, 2009. **16**(4): p. 1208-1220.

29. Witek, L., *Numerical stress and crack initiation analysis of the compressor blades after foreign object damage subjected to high-cycle fatigue.* Engineering Failure Analysis. **In Press, Accepted Manuscript**.

30. Salio, M., T. Berruti, and G. De Poli, *Prediction of residual stress distribution after turning in turbine disks.* International Journal of Mechanical Sciences, 2006. **48**(9): p. 976-984.

31. Silva, J.M., et al., *Creep-fatigue behavior of a new generation Ni-base superalloy for aeroengine usage.* Procedia Engineering, 2010. **2**(1): p. 1865-1875.

32. Sherby, O.D. and J. Weertman, *Diffusion-controlled dislocation creep: a defense.* Acta Metallurgica, 1979. **27**(3): p. 387-400.

33. Li, W., et al., *Residual stresses in face finish turning of high strength nickel-based superalloy.* Journal of Materials Processing Technology, 2009. **209**(10): p. 4896-4902.

34. Silveira, E., G. Atxaga, and A.M. Irisarri, *Influence of the level of damage on the high temperature fatigue life of an aircraft turbine disc.* Engineering Failure Analysis, 2009. **16**(2): p. 578-584.

35. Tjiptowidjojo, Y., et al., *Microstructure-sensitive notch root analysis for dwell fatigue in Ni-base superalloys.* International Journal of Fatigue, 2009. **31**(3): p. 515-525.

36. Hussain, K., D.S. Wilkinson, and J.D. Embury, *Effect of surface finish on high temperature fatigue of a nickel based super alloy.* International Journal of Fatigue, 2009. **31**(4): p. 743-750.

37. Evans, A., et al., *Relaxation of residual stress in shot peened Udimet 720Li under high temperature isothermal fatigue.* International Journal of Fatigue, 2005. **27**(10-12): p. 1530-1534.

38. Withers, P.J. and H. Bhadeshia, *Overview - Residual stress part 1 - Measurement techniques.* Materials Science and Technology, 2001. **17**(4): p. 355-365.

39. Ezeilo, A.N. and G.A. Webster, *Advances in Neutron Diffraction for Engineering Residual Stress Measurements.* Textures and Microstructures, 1999. **33**(1-4): p. 151-171.

40. Withers, P.J. and H. Bhadeshia, *Overview - Residual stress part 2 - Nature and origins.* Materials Science and Technology, 2001. **17**(4): p. 366-375.

41. Millwater, H., J. Larsen, and R. John, *Effects of residual stresses on probabilistic lifing of engine disk materials.* Materials Science and Engineering: A, 2007. **468-470**: p. 129-136.

42. Pawade, R.S., S.S. Joshi, and P.K. Brahmankar, *Effect of machining parameters and cutting edge geometry on surface integrity of high-speed turned Inconel 718.* International Journal of Machine Tools and Manufacture, 2008. **48**(1): p. 15-28.

43. Kwong, J., et al., *Minor cutting edge workpiece interactions in drilling of an advanced nickel-based superalloy.* International Journal of Machine Tools and Manufacture, 2009. **49**(7-8): p. 645-658.

44. Helm, D. and O. Roder, *Influence of long term exposure in air on microstructure, surface stability and mechanical properties of Udimet 720LI* in *Ninth International Symposium on Superalloys*. 2000: Seven Springs, PA; USA. p. 487-493.

45. Matsui, T., et al., *The Microstructure Prediction of Alloy 720LI for Turbine Disk Applications*, in *Ninth International Symposium on Superalloys*. 2000: Seven Springs, PA; USA. p. 127-133.

46. Reed, R., M. Jackson, and Y. Na, *Characterization and modeling of the precipitation of the sigma phase in UDIMET 720 and UDIMET 720Li.* Metallurgical and Materials Transactions A, 1999. **30**(3): p. 521-533.

47. Huang, Y.M., et al., *Micrometre scale residual stress measurement in fusion boundary of dissimilar steel welded joints using nanoindenter system.* Materials Science and Technology, 2011. **27**(9): p. 1453-1460.